

1 GEMS ozone profile retrieval: impact and validation of version 2 3.0 improvements

3 Juseon Bak¹, Arno Keppens², Daesung Choi³, Sungjae Hong³, Jae-Hwan Kim³, Cheol-Hee Kim³, Hyo-
4 Jung Lee³, Wonbae Jeon³, Jhoon Kim⁴, Ja-Ho Koo⁴, Joowan Kim⁵, Kanghyun Baek⁶, Kai Yang⁶ Yang⁷,
5 Xiong Liu⁷ Liu⁸, Gonzalo G. Abad⁷ Abad⁸, Klaus-Peter Heue⁸ Heue⁹, Jean-Christopher
6 Lambert² Lambert⁹², Yeonjin Jung⁹ Jung¹⁰, Hyunkee Hong¹⁰ Hong¹¹, Won-Jin Lee¹⁰ Lee¹¹

7 ¹Institute of Environmental Studies, Pusan National University, Busan 46241, Republic of Korea

8 ²Royal Belgian Institute for Space Aeronomy (BIRA-IASB), Brussels, Belgium

9 ³Department of Atmospheric Sciences, Pusan National University, Busan 46241, South Korea

10 ⁴Department of Atmospheric Sciences, Yonsei University, Seoul, Republic of Korea

11 ⁵Department of Atmospheric Sciences, Kongju National University, Kongju, Republic of Korea

12 ⁶[NASA Goddard Space Flight Center, Greenbelt, Maryland, USA](#)

13 ⁷[Department of Atmospheric and Oceanic Science, University of Maryland, College Park, MD 20742, USA](#)

14 ⁸[Smithsonian Astrophysical Observatory \(SAO\), Center for Astrophysics | Harvard & Smithsonian, Cambridge, MA 02138,
15 USA](#)

16 ⁹[Institut für Methodik der Fernerkundung am Deutschen Zentrum für Luft- und Raumfahrt \(DLR\), Oberpfaffenhofen,
17 Germany](#)

18 ¹⁰[Major of Spatial Information Engineering, Division of Earth and Environmental System Sciences, Pukyong National
19 University, Busan, Republic of Korea](#)

20 ¹¹[National Institute of Environmental Research, Incheon 22689, Republic of Korea](#)

22 *Correspondence to:* Juseon Bak (juseonbak@pusan.ac.kr), Jaehwan Kim (jaekim@pusan.ac.kr)

23 **Abstract.** This study presents the first comprehensive description of the operational GEMS (Geostationary Environment
24 Monitoring Spectrometer) ozone profile retrieval algorithm and evaluates the performance of the ~~recently~~ reprocessed version
25 3.0 dataset. The retrieval operates in the 310–330 nm spectral range and yields total degrees of freedom for ozone ranging
26 from 1.5 to 3. Although the vertical sensitivity is limited, GEMS achieves an effective vertical resolution of 5–10 km and is
27 capable of separating tropospheric and stratospheric ozone layers. This work ~~primarily~~ highlights ~~the substantial~~significant
28 algorithmic and calibration ~~enhancements~~ improvements ~~introduced~~ introduced in version 3.0 ~~over the previous version~~,
29 ~~including improvements to the slit function, wavelength calibration, and radiometric calibration. In particular, the radiometric~~
30 ~~offsets in irradiance measurements~~ are corrected using a scaling factor derived from the average ratio to a solar reference,
31 ~~while~~ In particular, the irradiance offset has been a major issue affecting the accuracy of ozone profile and other Level 2
32 ~~products. To address this, the measured irradiance is scaled relative to a high resolution solar reference spectrum using a~~
33 ~~correction factor. Residual residual~~ wavelength-dependent biases in the normalized radiance are further ~~addressed~~ mitigated
34 through soft calibration. In addition, wavelength shift corrections are applied separately to irradiance and radiance wavelengths.
35 As a result, version 3.0 significantly reduces spectral fitting residuals, lowering them from 0.8% in version 2.0 to 0.2% under
36 nominal conditions. This improvement also mitigates altitude-dependent oscillating biases observed in the previous version

(+40 DU in the troposphere, -20 DU in the stratosphere). The version 3 ozone profiles show agreements within ± 10 DU of ozonesonde observations, with a mean bias of -7.7% in tropospheric ozone columns and within 5% in the stratosphere. This improvement also mitigates the altitude dependent oscillating biases observed in the previous version, which included up to 40 DU overestimation in the troposphere and 20 DU underestimation in the stratosphere, when compared with ozonesonde observations. The version 3 ozone profiles show agreement within 10 DU of ozonesonde profiles, with a mean bias of -7.7% in tropospheric ozone columns and within 5% in the stratosphere. Furthermore, the retrievals capture day-to-day vertical ozone variability, as demonstrated by comparisons with daily ozonesonde launches in February and March 2024. Integrated ozone columns derived from the profiles also show improved consistency with ground-based total ozone measurements, yielding a mean bias of -3.6 DU and outperforming the GEMS operational total column ozone product.

1 Introduction

Atmospheric ozone is a powerful greenhouse gas and air pollutant, harming human health and ecosystems in the troposphere (Van Dingenen et al., 2009; Isaksen et al., 2009). In the stratosphere, ozone is essential for protecting life on Earth by absorbing harmful ultraviolet (UV) radiation from the Sun (Solomon, 1999). It also plays a key role in maintaining the Earth's radiative balance and stratospheric temperature structure (Monks et al., 2015). Monitoring both layers is vital for understanding pollutant transport, regulating air quality, addressing climate change, and protecting environmental health.

The Geostationary Environmental Monitoring Spectrometer (GEMS) onboard the Korean GEO-KOMPSAT(Geostationary Korea Multi-Purpose Satellite)-2B satellite provides high temporal and spatial resolution data on ozone, its precursors (NO_2 and HCHO), SO_2 , and aerosols over East Asia (Kim et al., 2020). GEMS offers two primary ozone products: total column ozone (O_3T) and the full ozone profile (O_3P). The O_3T product is retrieved using the historical TOMS look-up table algorithm (Kim et al., 2024), while the O_3P product provides vertically resolved ozone information across 24 atmospheric layers, retrieved based on an optimal estimation-based inversion framework (Bak et al., 2020). A comprehensive evaluation of GEMS v2.0 O_3T product has been conducted by (Baek et al., (2023, 2024)). Baek et al. (2023, 2024) provided a comprehensive evaluation of the GEMS v2.0 O_3T product, examining assessing its spatial and temporal representativeness on hourly, daily, and seasonal scales through cross-comparisons with ground-based Pandora measurements and independent satellite observations from polar-orbiting platforms. The product exhibited revealed strong correlations with Pandora (0.97) and satellite data (0.99), but showed a pronounced seasonal and latitudinal dependence in mean bias, which was attributed to attributed to the absence of a calibration component accounting for the bidirectional transmittance distribution function (BTDF) in irradiance measurements (Kang et al., 2024). A minor update to the look-up table was subsequently implemented, resulting in the release of version 2.1 (Kim et al., 2024). Although the GEMS O_3P product has not yet been fully described in peer-reviewed literature, the algorithm implemented for processing version 2.0 closely follows the Smithsonian Astrophysical Observatory (SAO) ozone profile algorithm used for generating the Ozone Monitoring Instrument (OMI) Collection 3 ozone

70 profile research product (Liu et al., 2010). The OMI ozone profile product has demonstrated its reliability in supporting studies
71 of ozone variability driven by the chemical and dynamical processes, quantifying global tropospheric budget of ozone, and
72 evaluating model representation (Bak et al., 2022; Hayashida et al., 2015; Kuang et al., 2017; Lu et al., 2018) (Hayashida et al.,
73 2015; Kuang et al., 2017; Lu et al., 2018; Hu et al., 2017; Bak et al. 2022). However, the project *Product Evaluation of GEMS*
74 *L2 via Assessment with S5P and Other Sensors (PEGASOS, funded by the European Space Agency)* reported the need for
75 improvements prior to scientific use, citing significant altitude-dependent oscillating biases in the GEMS O₃P version 2.0
76 product, with deviations of up to 30 % in the troposphere and from -10 % to -20% in the stratosphere
77 (<https://www.dlr.de/en/eoc/research-transfer/projects-missions/pegasos> Keppens et al., 2024). In addition, the PEGASOS
78 report identified large discrepancies between the GEMS O₃P and O₃T products. The inconsistencies in ozone profile quality
79 between GEMS and OMI can be attributed to differences in radiometric and wavelength calibration stability, rather than to the
80 retrieval algorithm itself, which shares similar forward and inverse processes.

81 These findings motivated the development of version 3.0 of the GEMS ozone profile product, which incorporates
82 improvements in spectral and radiometric calibration, including:

- 83 (1) ~~on-orbit derivation of updating of the pre flight measurements of~~ slit functions ~~to on orbit derivations,~~
- 84 (2) ~~correction of wavelength shift wavelength calibration in of~~ both radiance and irradiance spectra,
- 85 (3) ~~implementation of~~ irradiance offset correction to address solar diffuser-induced ~~seasonal variation angular~~
86 ~~dependence~~ and long-term optical degradation, ~~and and~~
- 87 (4) ~~application of~~ soft calibration to correct residual radiometric biases in the normalized radiances.

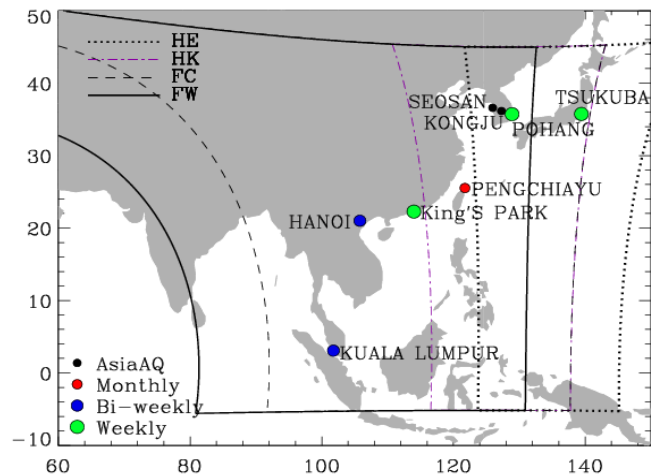
88 In addition to these calibration enhancements, the algorithmic updates include modifications to the forward model
89 calculations, fitting parameters, and several auxiliary inputs. This paper is structured around three main objectives. The
90 retrieval algorithm and the updates from version 2.0 to version 3.0 are introduced in the second section. Section 3 focuses on
91 retrieval characterization and error analysis based on optimal estimation diagnostics. Validation results using independent
92 reference datasets are discussed in Section 4. The final section concludes this paper, with remarks for future updates.

95 2. GEMS Ozone Profile Retrieval Algorithm

96 2.1 GEMS operations

97 GEMS is an ultraviolet-visible imaging spectrograph equipped with a single two-dimensional charge-coupled device (CCD)
98 array detector, with one dimension for 1,033 wavelengths and the other for 2,048 spatial pixels (Lee et al., 2024). It measures
99 solar irradiance once each night and Earth's backscattered radiance hourly from 07:45 to 16:45 Korea Standard Time (KST),
100 covering the spectral range from 300 to 500 nm with a spectral resolution of approximately 0.6 nm full width at half maximum

101 (FWHM). A shared optical path is used for both radiance and irradiance measurements, except for dedicated solar diffusers,
 102 which operate on different duty cycles (daily and monthly) to manage sunlight intensity and prevent detector saturation. In
 103 GEMS, ~~the~~ spatial pixels represent fixed ground-based observation points on Earth, aligned ~~along in~~ the north-south direction,
 104 ~~as viewed~~ from a geostationary orbit, ~~and~~ covering latitudes from 5°S to 45°SN. ~~These spatial pixels correspond to the, while~~
 105 ~~in polar orbiting satellites, the term "cross-track pixels" is typically used in polar-orbiting satellites, which reflecting their~~
 106 ~~spatial alignment are aligned~~ across the flight path. ~~For Earth observation, In Earth observation mode, GEMS scans an east-~~
 107 ~~west swath from 75°E to 145°E in approximately 700 mirror steps (scan lines) during in full-scan mode and 350 mirror steps~~
 108 ~~during in half-scan mode. Four scan modes — Half East (HE), Half Korea (HK), Full Central (FC), and Full West (FW) —~~
 109 are operated sequentially, with their spatial extents shown in Figure 1 and the detailed ~~operation~~ schedule summarized in
 110 Supplementary Tables 1 and 2. ~~The operational data record begins on November 2, 2020, The official data period began on~~
 111 ~~November 1, 2020 marking the start of the official observation period.~~ Currently, Version 2 Level 1C irradiance and Version
 112 1.2.4 radiance products ~~are are used as the standard Level 1C inputs for subsequent commonly used as inputs for~~ Level 2
 113 processing. To enhance computational efficiency and improve the signal-to-noise ratio, Level 1C and selected Level 2 products
 114 (e.g., cloud, surface reflectance, total ozone) are also ~~provided available~~ with spatial binning ~~of at~~ 2×2 or 4×4 pixels. The ozone
 115 profile retrieval specifically utilizes 4×4 binned data, resulting in a 512 × 175 frame dataset.



116
 117 **Figure 1. Geographic coverage of the four GEMS scan modes: Half East (HE), Half Korea (HK), Full Central (FC),**
 118 **and Full West (FW), indicated by the curved boundaries. Colored dots indicate ozonesonde stations with regular**
 119 **launches within the GEMS domain, classified by launch frequency: red for monthly, blue for bi-weekly, and green for**
 120 **weekly. Black dots represent additional sites that participated during the Asia-AQ campaign.**
 121

122 **2.2 Algorithm Heritage**

123 The heritage of the ozone profile retrieval algorithm is rooted in long-standing achievements efforts in to developing,
124 improving, and validating ozone profile retrievals from using satellite observation data spaceborne instruments such as from
125 the Global Ozone Monitoring Experiment (GOME), the OMI, the Ozone Mapping and Profiler Suite (OMPS), and the
126 Tropospheric Monitoring Instrument (TROPOMI) (Bak et al., 2017, 2024, 2025a; Cai et al., 2012; Dobber et al., 2008; Liu et
127 al., 2005, 2010; Zhao et al., 2021). The Optimal estimation technique (Rodgers, 2000) provides the theoretical foundation for
128 solving the inverse problem, enabling the transforming transformation of spectral information measurements into geophysical
129 data quantities. The retrieval process iteratively optimizes adjusts the atmospheric state vector to minimize the a cost function
130 that accounts for both the differences mismatch between simulated and measured spectra and the deviation of the state vector
131 from the a priori vector constraints. This optimization critically depends critically on stable wavelength and radiometric
132 calibration, as well as an accurate radiative transfer model, to ensure stable robust spectral fitting and reliable results.
133 Algorithmic updates from the OMI Version 2.0 research product by Bak et al. (2024) were adopted incorporated into the
134 development of the GEMS Version 3.0 ozone profile product. In addition, new calibration methodologies were implemented
135 for GEMS L1C radiance and irradiance were newly implemented to ensure spectral fitting stability and improve retrieval
136 accuracy. The following sections provide a detailed description of the inversion framework and its implementation.

137 **2.3 Optimal Estimation**

138 The Optimal Estimation-based inversion (Rodgers, 2000) is physically regularized toward minimizing the difference
139 between a measured spectrum Y and a spectrum that is simulated by the forward model $\mathbf{F}(X)$. Given an atmospheric state X ,
140 the X the inversion is constrained by the measurement error covariance matrix \mathbf{S}_y and statistically regularized by an a priori
141 state vector X_a with a priori covariance matrix \mathbf{S}_a . The cost function (chi-square) and the updated equation for the posterior
142 state vector X at iteration step $i + 1$ are written as

$$143 \chi^2 = \|\mathbf{S}_y^{-\frac{1}{2}}\{\mathbf{K}_i(X_{i+1} - X_i) - [Y - \mathbf{F}(X_i)]\}\|^2_2 + \|\mathbf{S}_a^{-\frac{1}{2}}(X_{i+1} - X_a)\|^2_2 \quad (1) \text{ and}$$

$$144 X_{i+1} = X_i + (\mathbf{K}_i^T \mathbf{S}_y^{-1} \mathbf{K}_i + \mathbf{S}_a^{-1})^{-1} [\mathbf{K}_i^T \mathbf{S}_y^{-1} (Y - \mathbf{F}(X_i)) - \mathbf{S}_a^{-1} (X_i - X_a)] \quad (2)$$

145 , where each component of the matrix \mathbf{K} is the derivative of the forward model to the actual atmospheric state, called the
146 Jacobians or weighting function matrix.
147

148 The posterior error covariance matrix, quantifying the total uncertainty in the retrieved state \hat{X} , is given by:

149 $\hat{\mathbf{S}} = (\mathbf{K}^T \mathbf{S}_y^{-1} \mathbf{K} + \mathbf{S}_a^{-1})^{-1}. \quad (3)$

150

151 The retrieval gain matrix \mathbf{G} , representing the sensitivity of the retrieval to the measurements, can be written as:

152 $\mathbf{G} = \hat{\mathbf{S}} \mathbf{K}^T \mathbf{S}_y^{-1} \quad (\mathbf{G} = \frac{\partial \hat{\mathbf{x}}}{\partial \mathbf{y}}). \quad (4)$

153 The product of \mathbf{G} and \mathbf{K} then yields the averaging kernel matrix \mathbf{A} , which characterizes the sensitivity of the retrieved state to
154 the true atmospheric state:

155 $\mathbf{A} = \mathbf{GK} \quad (\mathbf{A} = \frac{\partial \hat{\mathbf{x}}}{\partial x_{true}}). \quad (5)$

156 Beyond information content analysis, the matrices \mathbf{G} and \mathbf{A} also govern the retrieval error characteristics. Accordingly, $\hat{\mathbf{x}}$ can
157 be expressed as:

158 $\hat{\mathbf{x}} = \mathbf{Ax}_{true} + (\mathbf{I}_n - \mathbf{A})\mathbf{x}_a + \mathbf{G}\sigma_y \quad (6)$

159 which represents a weighted combination of the true atmospheric state and a priori information, and adds the measurement
160 noise. The retrieval uncertainty due to measurement noise is quantified by propagating σ_y from the measurement space into
161 the state space through the gain matrix \mathbf{G} , resulting into the measurement error covariance matrix:

162 $\mathbf{S}_n = \mathbf{GS}_y\mathbf{G}^T. \quad (7)$

163 Meanwhile, the smoothing error covariance matrix, representing the retrieval uncertainty caused by limited vertical
164 information, is defined as:

165 $\mathbf{S}_s = (\mathbf{A} - \mathbf{I})\mathbf{S}_a(\mathbf{A} - \mathbf{I})^T \quad (8)$

166 These two contributions then add up to the total covariance as given in Eq. (3), or $\hat{\mathbf{S}} = (\mathbf{I} - \mathbf{A})\mathbf{S}_a$.

167 2.4 Implementation details [and algorithm updates](#)

168 The state vector \mathbf{X} includes 24 partial ozone columns, surface albedo (0th and 1st order wavelength terms), cloud fraction,
169 and six additional calibration parameters (see Supplementary Table 3). The measurement vector \mathbf{Y} consists of the logarithms
170 of the sun-normalized radiance spectra, which enhances retrieval stability by reducing the sensitivity to absolute radiance errors
171 and Fraunhofer lines. Measurement errors (σ_y) are assumed to be mutually uncorrelated. Since the GEMS L1C product does
172 not provide measurement error estimates, a constant relative error of 0.2% is uniformly applied across the spectral range.
173 Accordingly, the measurement error covariance matrix is defined as:

174 $\mathbf{S}_y = \text{diag}(\sigma_{y,1}^2, \sigma_{y,2}^2, \dots, \sigma_{y,n}^2).$

175 Correlations between ozone layers are accounted for using a correlation length L of 6 km in the a priori error covariance matrix
176 using a correlation length L of 6 km, defined as:

177 $\mathbf{S}_a = \sigma_i^a \sigma_j^a \exp(-(|i - j| / L)^2),$

178 where σ_i^a and σ_j^a are the a priori errors of the i^{th} and j^{th} state vector components of the state vector, respectively. The updates

179 from GEMS v2.0 to v3.0 mirror those from OMI v1.0 to v2.0. In particular, the radiative transfer model is replaced with the
180 PCA-VLIDORT v2.6 (Bak et al., 2021) to enhance the simulation efficiency. A look-up table correction was also ~~newly~~
181 implemented to account for approximations in the radiative transfer calculation related to the number of streams, coarse vertical
182 layering, and polarization treatment. The TSIS-1 Hybrid Solar Reference Spectrum (Coddington et al., 2021) is now used
183 instead of the solar reference from Chance and Kurucz (2010). The ozone cross-section has been ~~changed~~~~switched~~ from BDM
184 1995 (Brion et al., 1993; Daumont et al., 1992; Malicet et al., 1995) to BW ~~2018~~ (Birk and Wagner, 2018). Notably, the a
185 priori ozone profile, based on the tropopause-based ozone climatology (Bak et al., 2013), has been consistently used in GEMS
186 v2.0, GEMS v3.0, and OMI v2.0. The temperature data are necessary to account for the temperature dependence of the ozone
187 cross-section, while surface and tropopause pressures are used to define the 25-level pressure grids (Supplementary Fig. 1).
188 The tropopause pressure is also used to convert the a priori ozone profile from a tropopause-based to a surface-based vertical
189 coordinate system. For meteorological inputs, the Global Forecast System (GFS) of a National Centers for Environmental
190 Prediction (NCEP) weather forecast model is used in the daytime processing (DRPO) mode. GFS data are downloaded daily
191 at 05:00 KST, covering forecast periods between 6 KST and 18 KST, with lead times of 12 to 21 hours. In the reprocessing
192 (RPRO) mode, the meteorological input is switched to the NCEP FNL (Final) Operational Global Analysis data. The
193 meteorological fields, provided at 3-hour intervals (GFS) or 6-hour intervals (FNL) per day, are interpolated to match the
194 GEMS reference time ~~(HH:45)~~.

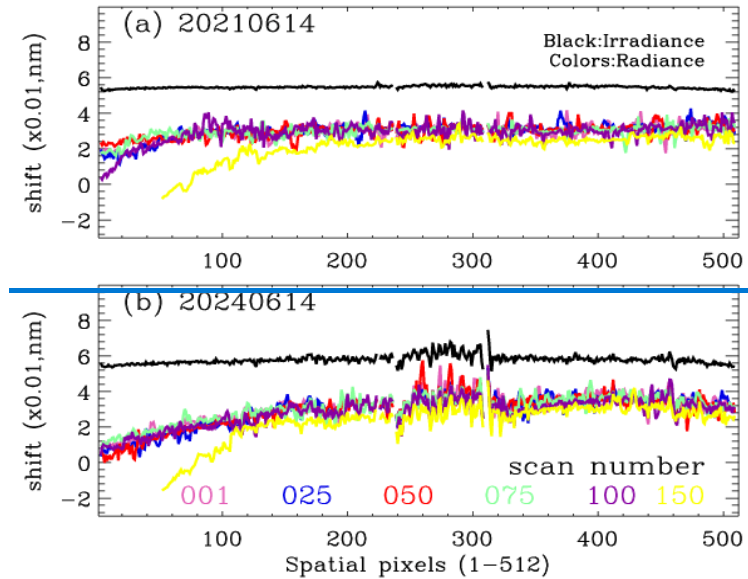
195 2.5 Calibration methodologies

196 The calibration process consists of several key components: on-orbit slit function derivation and wavelength calibration
197 to ensure spectral accuracy (Section 2.5.1), as well as irradiance offset correction and soft calibration to reduce radiometric
198 uncertainties (Section 2.5.2).

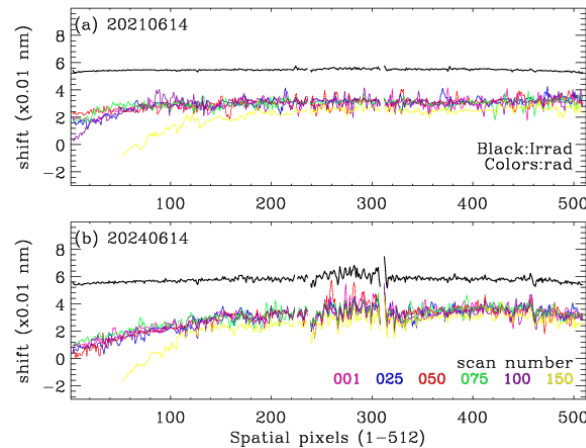
200 2.5.1 ~~spectral~~Spectral correction

201 The instrument spectral response function (ISRF), or slit function is required to degrade high-resolution spectra (e.g.,
202 absorption cross-sections) to match the spectral resolution of GEMS. Pre-flight ISRFs, measured at six discrete wavelengths
203 and interpolated across all 1,322 wavelength grids, are available (Kang et al., 2022). However, our companion study proposes
204 an on-orbit slit function derivation for GEMS based on a super-Gaussian model to account for temporal variations in the
205 instrument response (Bak et al. 2025b), and is therefore not repeated here. That study also ~~reports~~~~indicated~~ that the irradiance
206 spectrum should be shifted by 0.055 nm to align with the Fraunhofer lines. In Most~~most~~ GEMS Level 2 trace gas algorithms-
207 ~~the irradiance-derived shift is applied directly to the radiance spectra, assume under the assumption that similar the~~ spectral
208 shifts for radiance and irradiance ~~are similar, applying the irradiance derived shift directly to the radiance spectra.~~ However,
209 ~~as shown in Figure 2, substantial discrepancies are evident in Figure 2 reveals substantial discrepancies in~~ both the magnitude

210 and spatial pattern of the spectral shift between radiance and irradiance, ranging from 0.02 to 0.04 nm, with larger differences,
 211 with larger differences observed toward the northern edge of the spatial domain. Additionally, as degradation progresses, pixel-
 212 to-pixel perturbations increase toward the central spatial pixels in both radiance and irradiance measurements.
 213 ThereforeTherefore, independent shift correction is implemented to radiance and irradiance. To ensure computational
 214 efficiency in operational processing, the radiance shift is determined from the first mirror step and applied uniformly along the
 215 scan direction, based on the observation that spectral shifts in the radiance data remain relatively uniform across mirror steps.
 216 Additionally, as degradation progresses, pixel to pixel perturbations increase toward the central spatial pixels in both radiance
 217 and irradiance measurements.



218



219

220
221 **Figure 2. Shifts of irradiance and radiance relative to the solar reference from Coddington et al. (2021), shown as a**
222 **function of spatial pixel number (1–512) for (a) June 14, 2021 (20210614) and (b) June 14, 2024 (20240614).** Colored
223 lines represent the scan lines (mirror steps) plotted at 25-intervals, ranging from 1 to 150.

224 **2.5.2 Radiometric correction**

225 The GEMS irradiance is spatially and seasonally biased due to a missing calibration component for the BTDF, which
226 defines how light transmits through a diffuser based on incident and outgoing angles—a well-known issue (Kang et al. 2024;
227 Bak et al. 2025b). Additionally, Bak et al. (2025b) identified progressive radiometric degradation, resulting in an annual
228 irradiance decrease of ~5% in the shorter UV range. They also reported that the measured irradiance is roughly 40% lower
229 than the solar reference near 325 nm. Because normalized radiance is used in spectral fitting, such irradiance biases can directly
230 propagate into retrieval output. To address these discrepancies, a major revision was implemented in version 3. Specifically, a
231 sealing correction factor was introduced to compensate for the systematic difference between the GEMS irradiance (I_m) and a
232 high-resolution solar reference spectrum (I_{ref}). This correction factor (C) is derived by minimizing the following cost function:

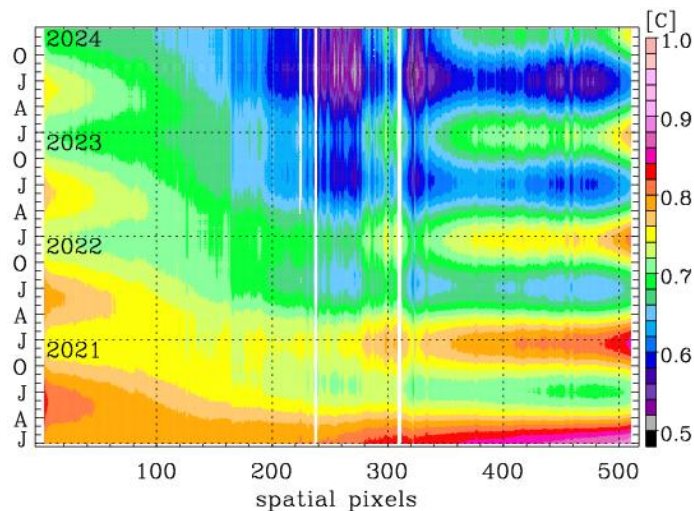
233
$$\chi^2 = \sum_{\lambda} (I_m(\lambda) - [C \cdot I_{ref}(\lambda + \Delta \lambda) \otimes S + \sum_m^3 P_b^m (\lambda - \bar{\lambda})^m])^2 \quad (9)$$

234 where:

235 • S: instrument spectral response function (ISRF)
236 • \otimes : convolution operator,
237 • $\Delta \lambda$: wavelength shift
238 • P_b^m : coefficients of a third-order baseline polynomial centered at $\bar{\lambda}$

239
240 In this approach, the slit function parameters and the wavelength shift are first determined independently and then held fixed,
241 allowing the solar reference spectrum to be adjusted to the measured irradiance in terms of spectral resolution and spectral
242 alignment. The scaling factor C and the baseline polynomial P_b are subsequently fitted to capture remaining radiometric
243 differences. As presented in Figure 3, the derived values of C exhibit significant seasonal and spatial variations in irradiance
244 offset related to angular dependence, along with a gradual temporal decline attributable to optical component degradation,
245 particularly most prominently at the middle spatial pixels. In version 3, only the scaling factor C is applied in the irradiance
246 correction, by dividing the irradiance by C . This decision was made because applying the baseline polynomial P_b directly to
247 the irradiance introduced artificial structures into the spectral fitting of the normalized radiance, resulting in a significant
248 underestimation of stratospheric ozone retrievals. Residual wavelength-dependent uncertainties are instead addressed through

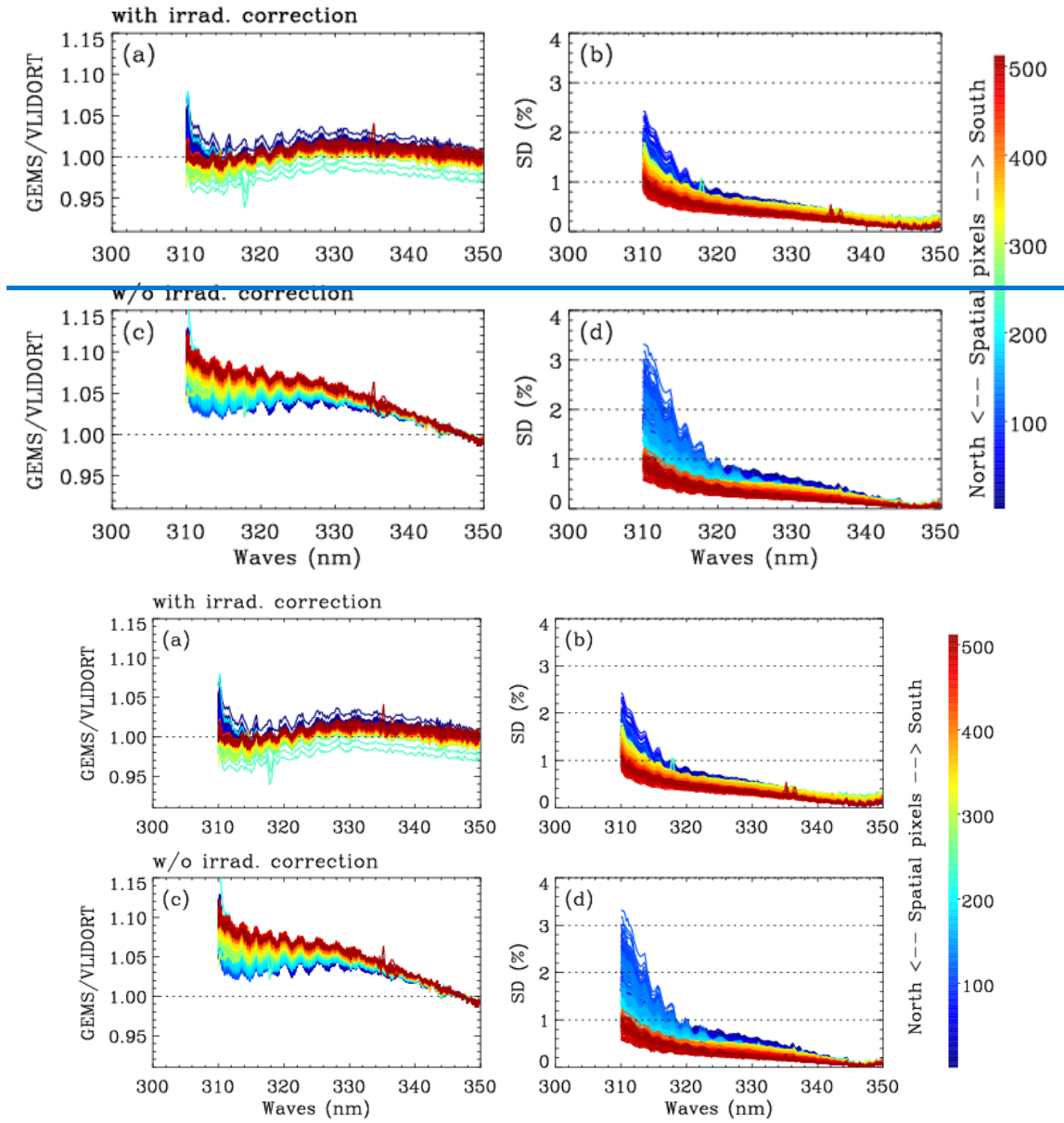
249 the soft calibration process, which has been newly implemented in version 3. This empirical correction eliminates systematic
 250 biases in the normalized radiance by applying adjustment factors derived from the ratio of measurements to simulated spectra
 251 based on accurate forward model calculations. The ozone profile input for the forward model calculation is constructed using
 252 daily zonal mean Microwave Limb Sounder (MLS) data (Livesey et al., 2025) above 215 hPa and climatological profiles
 253 (McPeters and Labow, 2012) below that level, with the integrated total column adjusted to match the zonal mean total ozone
 254 from daily OMPS measurements (Jaross, 2017). A one-week set of clear sky measurements, collected at 02:45 UTC between
 255 July 11 and 17, 2021, is used to derive the soft calibration spectra as a function of the 512 spatial pixels. While a cloud fraction
 256 threshold of 0.2 is typically used to define clear-sky conditions, we relaxed this criterion to 0.4 due to the known overestimation
 257 in the GEMS cloud product, which is also affected by irradiance offsets. Figure 4 illustrates the derived soft spectra and the
 258 impact of applying the irradiance correction. After correction, the soft calibration spectra show significantly reduced biases
 259 and improved spatial consistency. The residual biases are generally positive and remain below 3% for most pixels, except for
 260 a few central pixels that exhibit negative values, possibly due to unflagged dead pixels in the GEMS L1C data. In contrast,
 261 without the correction, substantial wavelength-and spatially dependent biases are evident, with systematic biases ranging from
 262 3% to 10% in the shorter UV range. Moreover, the standard deviation of the residual spectra stays below 1% for spatial pixels
 263 numbered below 100, while it increases above 3% for pixels above 400 without correction. With correction applied, this
 264 increase is limited to 2 %. Figure 5 demonstrates the resulting improvement in spectral fitting accuracy achieved through the
 265 application of both radiometric (scaling correction to irradiance and soft calibration to normalized radiance) and wavelength
 266 calibration in version 3, compared to version 2. With these corrections, mean fitting residuals decreased from approximately
 267 0.8% in v2.0 to 0.2% in v3.0 across most spatial pixels, representing more than a fourfold enhancement in retrieval precision.
 268 Version 3.0 not only reduces the mean fitting residuals but also achieves substantial improvements in seasonal stability, spatial
 269 uniformity, and the removal of systematic and random artifacts, —highlighting the effectiveness of the enhanced calibration
 270 and retrieval procedures.



271

272
273
274

Figure 3. Time–space distribution of the derived **sealing**–correction factor C across 512 spatial pixels from January 2021 to December 2024. The **sealing**–factor C, fitted over the 310–330 nm spectral window, represents the ratio **of** **between**–GEMS irradiance **and**–**to** a high-resolution solar reference spectrum.



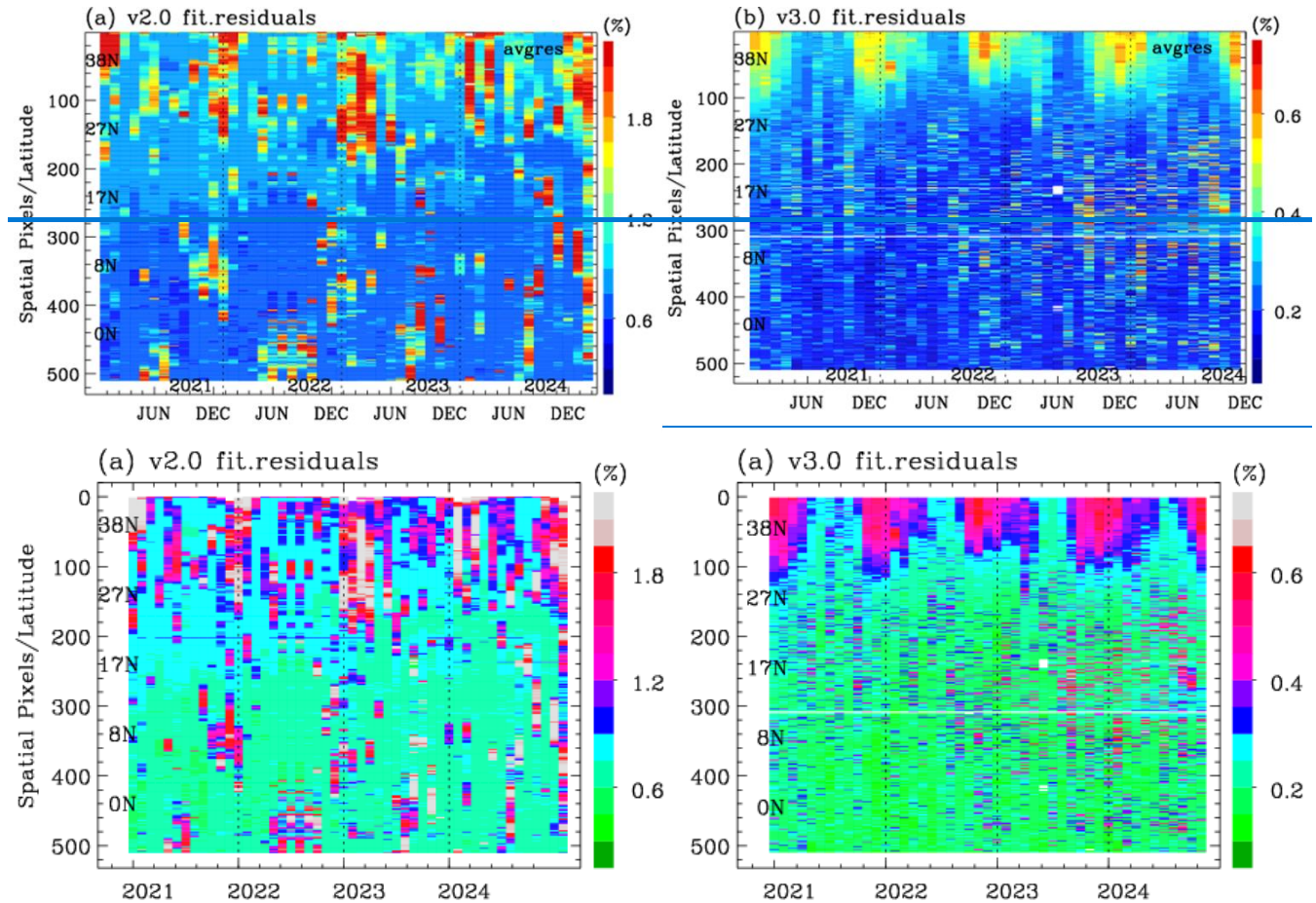
275

276
277
278

Figure 4. GEMS soft spectrum, derived as the mean difference between measured and simulated normalized radiances, as a function of wavelength (300–350 nm) for each of the 512 spatial pixels (color-coded from north to south), with the

279
280

standard deviation of the mean difference. The upper panel includes the scaling correction for the irradiance offset, while the bottom panel does not.



283
284
285
286
287
288
289
290
291
292
293
294
295

Figure 5. Comparison of spectral fitting quality from ozone profile retrievals between versions 2.0 and 3.0, averaged over the first 20 scanlines and shown as a function of the 512 spatial pixels. The evaluation is performed on the 15th day of each month from 2021 to 2024 (04:45 UTC). Fitting residuals, calculated as the root mean square (RMS) of the relative differences between measured and simulated radiance (%), are stored as “ResidualOffit” in version 2 and “avg_residuals” in version 3. Note that the color scale range in panel (b) is narrowed to one-third of panel (a) to enhance the visibility of the lower residual values.

3. Retrieval Characterization

The retrieved ozone profiles can be characterized by their information content and associated uncertainties, assessed using the averaging kernel matrix (AKM) and error covariance matrix (CVM) are used to characterize the retrieval sensitivity and its associated uncertainties for each profile. These Their characteristics are primarily mainly influenced governed by the

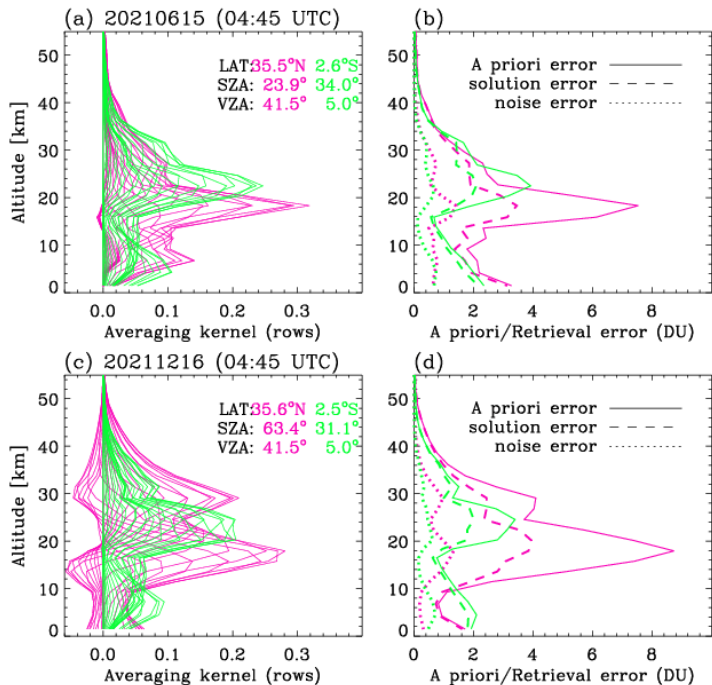
296 choice of fitting window, measurement noise, and the a priori covariance matrix, and they remain largely unchanged unchanged
297 between versions 2 and version 3 of the retrieval algorithm. The rows of the AKM serve as vertical smoothing functions,
298 indicating representing the sensitivity of the retrieved ozone concentration to changes in the true atmospheric state (see Eq. 5).
299 The trace of the AKM, referred as yields the degrees of freedom in for the signal (DFS), quantifies representing the total
300 number of independent pieces of information available from the in the retrieval measurements. DFS can also be calculated for
301 specific vertical sub columns using partial traces. Retrieval uncertainty, given by the square root of the CVM diagonal, is
302 assessed relative to against the a priori uncertainty, considering both the total error and the contribution from measurement
303 noise alone both in terms of total uncertainties and the contribution from measurement noise alone.

304 Figure 6 shows average the mean averaging kernels and uncertainty profiles from the GEMS 04:45 UTC scans, covering
305 two regions with different viewing zenith angles (VZA) and two dates with different solar zenith angles (SZA).

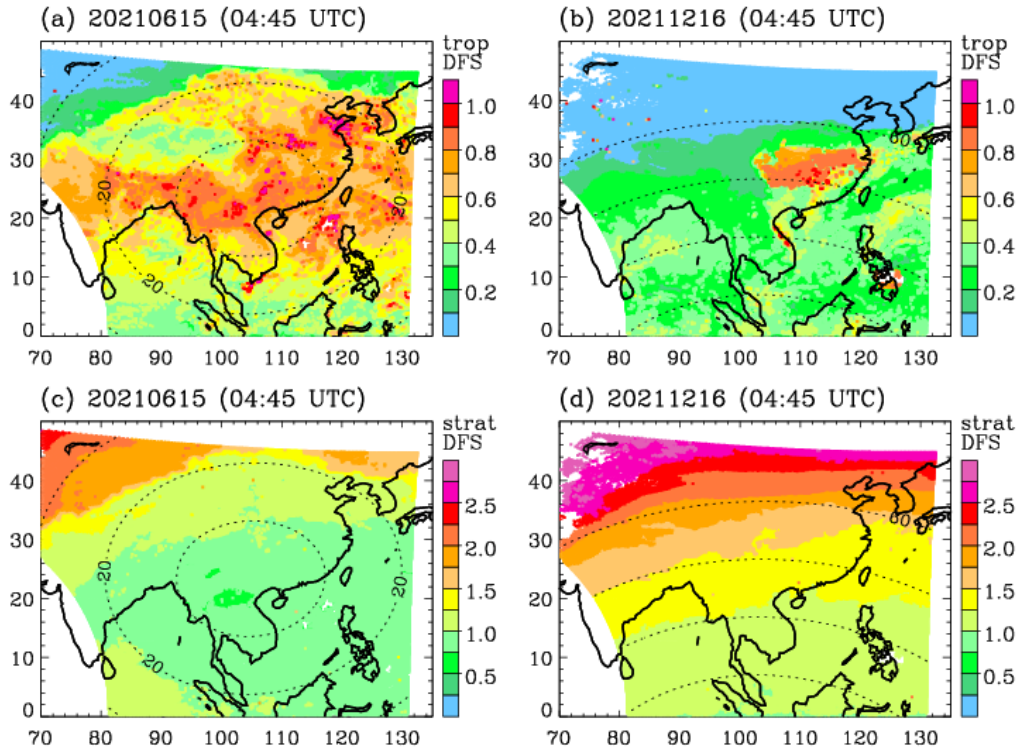
309 The averaging kernels peak notably just below the stratospheric ozone layer and within the upper troposphere–lower
310 stratosphere (UTLS), where the a priori uncertainty is largest, indicating that the retrieval provides the greatest information
311 content from the GEMS 04:45 UTC scan on 15 June and 16 December 2021, for two observation locations with different
312 optical paths determined by solar zenith angles (SZA) and viewing zenith angles (VZA). The retrieval typically yields the most
313 information (highest averaging kernel peaks) where the a priori uncertainty is highest, notably just below the stratospheric
314 ozone layer and in the upper troposphere and lower stratosphere (UTLS). The vertical location of these maxima peaks is,
315 however, strongly depends influenced by the on the optical path length (SZA and VZA). At the kernel peaks, the retrieval
316 uncertainty is reduced by ~ 50 % with respect to the a priori, with about one-third of the solution total (solution) error being
317 due to measurement noise. Away from the peaks, the reduction in uncertainty is generally smaller. At high SZAs, negative
318 kernel oscillations are evident, indicating reflecting challenges in vertically allocating the measurement information. This
319 suggest that the retrieval may offer only limited improvement over the prior under such conditions.

320 Figure 7 presents the sub-columns DFS values for the troposphere and stratosphere, based on the same observation cases
321 shown in Figure 6. The corresponding ozone partial columns are also included provided in (Supplementary Fig. 2), reflecting
322 the expected dependence of information content on atmospheric ozone concentration, given the expected dependence of the
323 information content on the atmospheric ozone concentration. The stratospheric DFS clearly increases with optical path lengths,
324 and thus with latitude (Fig. 7.c, d), especially winter (Fig. 7d), whereas the tropospheric DFS In the troposphere, the effect of
325 optical path length is weaker and only apparent at higher latitudes, she shows the opposite behaviour, with higher values
326 at lower SZA/VZA: DFS values decrease with increasing SZA and VZA (Fig. 7e). This relationship becomes
327 more complex by factors such as tropospheric ozone abundance, surface reflectance, and other scene-dependent characteristics
328 including aerosol and clouds. In the summer case, the tropospheric DFS indicates that the Additionally, there is a strong
329 correlation with the tropospheric ozone burden: the retrieval yields more information when ozone concentrations are higher,

330 resulting in stronger absorption signals (0.5-1.0 DFS). In the December case, tropospheric DFS values generally range from
 331 0.2 to 0.5 at latitudes below 30°. Abnormally high DFS values (0.7-0.9) are linked to elevated surface albedo, retrieved as a
 332 compensation for missing cloud information in pixels where the GEMS Level 2 cloud product fails to provide valid output
 333 (Supplementary Fig. 3). Adding up Summing the tropospheric and stratospheric DFS contributions, the total DFS typically
 334 ranges from 1.5 to 3, with a somewhat compensating effect observed at higher latitudes, where decreases in tropospheric DFS
 335 are offset by increases in stratospheric DFS. between tropospheric decreases and stratospheric increases for the higher latitudes.
 336



337
 338 **Figure 6. Averaging kernels and retrieval errors of ozone profiles from the GEMS 04:45 UTC scans on 15 June (a, b, c) and 16 December (b, d) 2021. The pink and green lines indicate averages over cross-track pixels 50-100 and 450-550, respectively, at the first scan line.**
 339
 340



342
 343 **Figure 7. Degrees of freedom for signal (DFS) for tropospheric column ozone on (a) 15 June and (b) 16 December 2021,**
 344 **and analogous for the stratospheric column in (c) and (d), respectively. Contours indicate the solar zenith angle (SZA)**
 345 **at 20° intervals. The corresponding ozone distributions are shown in Supplementary Figure 2.**

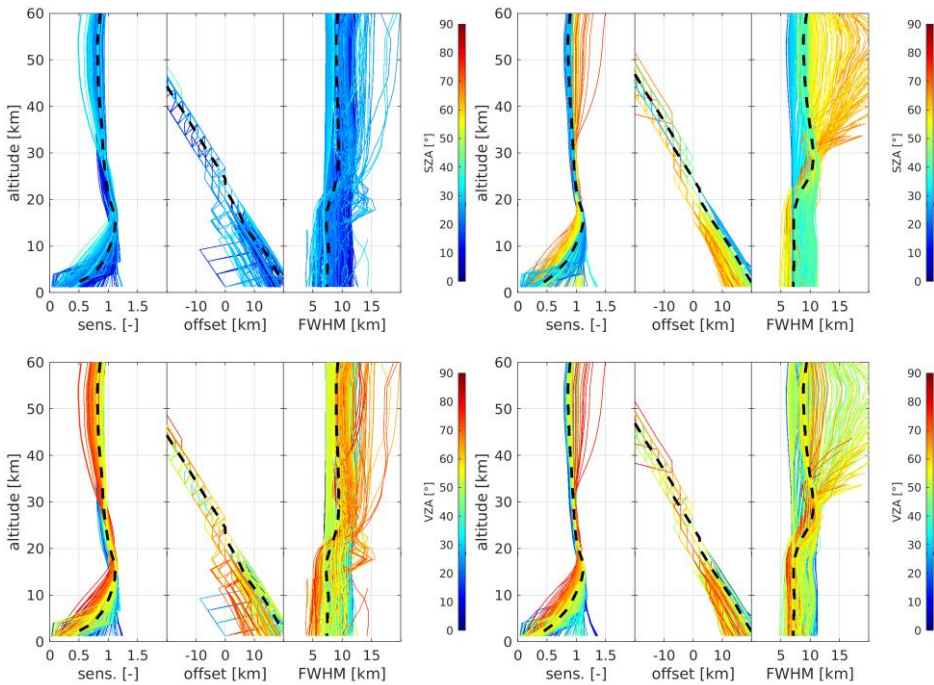
346
 347 In this work, we further examine three supplementary diagnostics: the retrieval sensitivity, retrieval offset and effective
 348 vertical resolution (which differs from the sampling resolution), following Keppens et al. (2015). The sum of each row of the
 349 AKM quantifies the total retrieval sensitivity, providing a vertically resolved and normalized measure of the contribution from
 350 satellite observations relative to the a priori profile. The retrieval offset indicates any vertical mismatch between the location
 351 of maximum sensitivity (the retrieval barycenter) and the nominal retrieval altitude (Rodgers, 2000). The effective vertical
 352 resolution is [derived from defined by](#) the [FWHM width](#) of each averaging kernel, [treated as a vertical smoothing function](#).
 353 [Here, we use the full width at half maximum \(FWHM\) as a measure of vertical resolution](#). This measure, however, does not
 354 [consider account for](#) averaging kernel oscillations, including the [presence occurrence](#) of negative values (see [Figure Fig. 6](#)).
 355 Figure 8 presents the retrieval diagnostics described above—sensitivity, offset, and vertical resolution—for GEMS ozone
 356 profile retrievals, evaluated from every tenth mirror step and spatial pixel, [yielding on the resulting in the order of 1000 profiles](#)
 357 [for per daily plot the \(89088/100 for the 04:45 UTC scan\)](#). [SZA and VZA are major quantities affecting the retrieval](#)
 358 [performance, while other influence quantities are examined in the Supplement](#). The results show that, on average, the vertical
 359 sensitivity of the [ezone profile](#) retrievals is close to unity throughout most of the profile. Sensitivity [decreased drops to values](#)

360 below 0.5 only in the lowest 5 km, with higher values occurring above highly reflective surfaces (e.g., including high cloud
361 fractions). -

363 ~~As expected, sensitivity drops significantly below clouds.~~ In the troposphere, vertical sensitivity generally increases with
364 ~~decreasing shorter optical paths length~~ (e.g., lower SZA and VZA), ~~which, as shorter paths~~ enhance atmospheric penetration.
365 In the stratosphere, however, higher sensitivities ~~are observed~~ occur under ~~for~~ more oblique viewing geometries (higher VZA),
366 particularly during winter when ~~large~~ SZAs ~~further increase enhance the DFS. are also high, resulting in increased DFS. In By~~
367 contrast, ~~during in~~ summer, when SZAs are ~~lower~~~~smaller~~, stratospheric sensitivity is ~~higher~~~~lower~~ for near-nadir viewing
368 angles (i.e., shorter path lengths).

369 Outside ~~of~~ the UTLS (about 15-30 km), the retrieval barycenter deviates ~~approximately nearly~~ linearly from the nominal
370 retrieval altitude. ~~This means that Consequently,~~ the vertical sensitivity is primarily distributed off-diagonal, with its barycenter
371 ~~located residing~~ in the UTLS (as can also be seen from the averaging kernel peak positions in Figure 6). ~~In the troposphere, -~~
372 ~~and results in a rather low average retrieval DFS (also see the sum of both partial DFS values in Figure 7). The~~ retrieval offset
373 depends on SZA and VZA (and ~~hence thus~~ latitude), ~~in the troposphere~~ but shows no other significant dependences on the
374 influence quantities ~~under study~~ examined (Supplementary Fig. 4). The offset ~~decrease under more oblique solar and viewing~~
375 ~~geometry, is reduced although this is accompanied by a reduction in tropospheric retrieval sensitivity. for more sideways solar~~
376 ~~irradiance and observation of the troposphere, although it has to be taken into account that the tropospheric retrieval sensitivity~~
377 ~~is at the same time reduced as well (see above).~~

379 The average effective vertical resolution of the GEMS ozone profiles ranges from 6 to 10 km, ~~with the highest values~~
380 ~~founded in the lower stratosphere~~. Both in the troposphere and stratosphere, ~~actual values against they~~ strongly depend on SZA
381 and VZA. ~~However, resulting in a meridian dependence as well, but again an~~ opposite behaviors ~~is are~~ observed above and
382 below the tropopause: ~~longer path lengths result in lead to~~ coarser vertical resolutions (~~reduced larger~~ FWHM) in the
383 troposphere, ~~while while in the stratosphere, especially under very high SZA, they result in finer vertical resolution, the~~
384 ~~opposite happens in the stratosphere, especially for very high SZA during winter, meaning the retrieved information is~~
385 ~~distributed over a larger vertical extent with the retrieved information distributed over a larger vertical extent.~~



386
387 **Figure 8: GEMS ozone profile retrieval information content in terms of sensitivity, offset, and kernel FWHM**
388 **for GEMS ozone profile retrievals on June 15 (left) and December 16 (right) 2021. Black dashed lines indicate median**
389 **values. Color coding represents, and for SZA (top) and VZA (bottom), which are the primary quantities influencing**
390 **retrieval characteristics; as physical influence quantities, color-coded in each plot. Median values are indicated by**
391 **black dashed lines; additional factors are presented in the Supplement.**
392

393 4. Validation using independent reference datasets

394 As a preliminary step in establishing a reliable validation framework for GEMS ozone profile retrievals, Bak et al. (2019)
395 evaluated ozonesonde soundings from 10 East Asian sites and and found that electrochemical concentration cell (ECC) sensors
396 provided more reliable measurements than than modified Brewer–Mast (MBM) and carbon–iodine (CI) sondes. They also
397 emphasized the importance of maintaining -consistent procedures across the preparation, operation, and post-processing stages
398 to ensure the long-term data quality and consistencyconsistency of data quality. Among these these sites, five—Pohang, Hong
399 KongKing’s Park, Tsukuba, Hanoi, and Kuala Lumpur—have remained active during the GEMS mission, regularly launching
400 balloon-borne ECC ozone sensors. Weekly regular observations have continued at Pohang, King’s Park, and Tsukuba in the
401 afternoon (1:30-2:30 pm LT). While Hanoi and Kuala Lumpur, where ozonesondes are launched provide bi-weekly
402 observations, they were not recommended as reference sites in Bak et al. (2019) due to because of frequent changes in either

403 the-sensing solution concentrations or the ozonesonde manufacturer. During the GEMS operational period, however, these
 404 inconsistencies have been better managed during the GEMS operational period, and thus the data from these sites are therefore
 405 included in this study. In addition, monthly ozonesonde observations from Pengchiayu, initiated which began in 2022, are also
 406 incorporated also incorporated. Table 1 summarizes the availability of the regular ozonesonde sites used for GEMS validation
 407 in Section 4.1. In Section 4.2, we additionally further use include a total of 13 ~~ECC~~ ozonesondes launched at Seosan (126.38°E,
 408 36.92°N) and 10 launched ~~in March~~ at Kongju (127.74°E, 36.47°N), South Korea, as part of the 2024 Airborne and Satellite
 409 Investigation of Asian Air Quality campaign (NASA, 2023). Integrated total ozone columns were also evaluated at Seosan
 410 during the ASIA-AQ campaign (Section 4.2) using Pandora measurements.

411 ~~These two sites, approximately 131 km apart, are marked by black symbols in Figure 1. Ozonesonde measurements can be~~
 412 ~~spatially matched with GEMS FW observations taken at 04:45 UTC, except for those from the Tsukuba station, which lies~~
 413 ~~outside the FW domain. Instead, the Tsukuba station falls within the coverage of the FC scan, which operates at 01:45, 02:45,~~
 414 ~~or 03:45 UTC, depending on the season. Integrated total ozone columns were also evaluated using Pandora measurements~~
 415 ~~(Herman et al., 2015) at Seosan during the ASIA-AQ campaign (Section 4.2).~~

417 **Table 1. List of regular ozonesonde stations used in this study.**

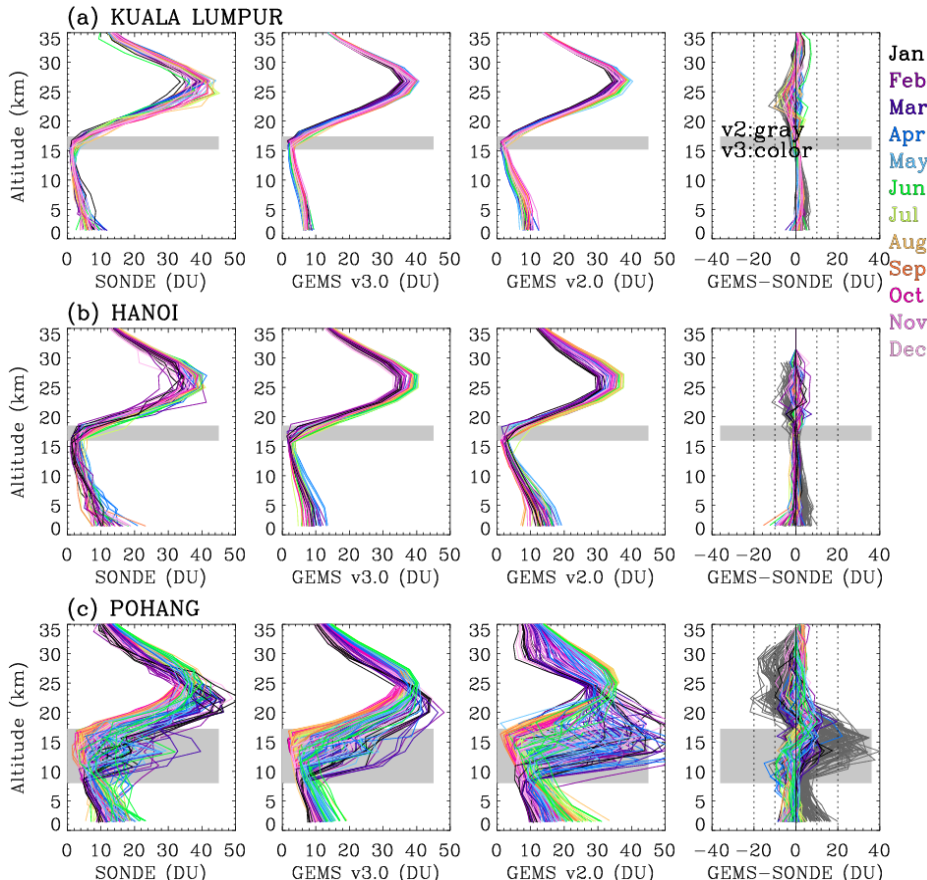
Station	Pohang	Tsukuba	King's park	Hanoi	Pengchiayu	Kuala Lumpur
Country	South Korea	Japan	Hong Kong	Vietnam	Taipei	Malaysia
Lon, Lon (deg.)	36.03, 129.38	36.06, 140.13	22.31, 114.17	21.02, 105.804	25.63, 122.08	2.73, 101.7
Provider [#]	KMA	WOUDC	WOUDC	SHADOZ	WOUDC	SHADOZ
Frequency	Weekly	Weekly	Weekly	Bi-weekly	Monthly	Bi-weekly
Launch Time (LT)	2:00 pm	2:30 pm	1:30 pm	1:00 pm	12:00 am	12: 30 am
Beginning date	1995-01-12	2017-06-22	2000-01-05	2004-09-18	2022-04-18	1998-05-04
Latest update	2024-06-26	2025-02-27	2024-12-31	2024-02-23	2024-05-12	2022-12-22

418 [#]KMA (Korea Meteorological Administration), WOUDC (World Ozone and Ultraviolet Radiation Data Centre), SHADOZ
 419 (Southern Hemisphere ADDitional OZonesondes)

422
423
424
425
426

427 **4.1 Validation with regular ozonesonde soundings**

428

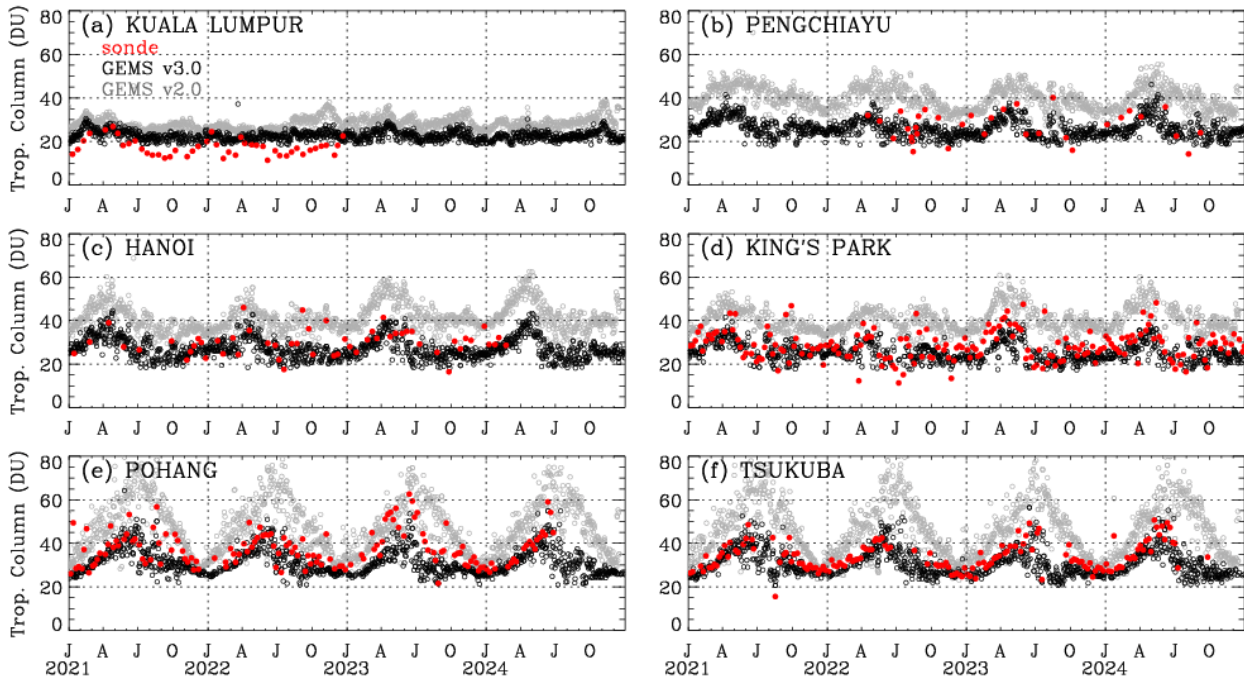


429

430 **Figure 9. Ozone vertical profiles (in DU) at three sites—(a) Kuala Lumpur, (b) Hanoi, and (c) Pohang—during 2021–
431 2024. Each panel displays individual ozonesonde soundings along with corresponding GEMS v3.0 and v2.0 retrievals.
432 The last columns present the respective differences (GEMS – SONDE) for GEMS v3.0 and v2.0, displayed in color and
433 dark gray, respectively. The gray shaded area denotes the range of tropopause altitudes (minimum to maximum).**
434

435 Ozonesondes are used to validate GEMS FW scan measurements from FW scans, which provide better temporal
436 coincidence in the afternoon (Table 1; Supplementary Tables 1-2). However, those from Tsukuba are matched with GEMS FC
437 scan measurements due to spatial constraints (See Fig. 1). Figure 9 illustrates how well GEMS captures the vertical distribution
438 of ozone up to 35 km—the typical burst altitude of ozonesonde balloons—at three stations representing different latitudinal
439 regionsbands: mid-latitudes (Pohang), subtropics (Hanoi), and tropics (Kuala Lumpur). The latest Compared to the previous
440 version, the updated GEMS v3.0 version (v3.0) demonstrates substantial improvements, in reproducing ozone vertical profiles,
441 particularly at the mid-latitude site of Pohang. Tropospheric ozone agreeagrees within 10 DU of ozonesonde measurements,
442 while stratospheric ozone is within 5 DU. However, GEMS v2.0 exhibited In GEMS v2.0, tropospheric ozone was
443 overestimated high biases in tropospheric ozone of by up to up to 20 DU, reaching 40 DU in the lower troposphere and by
444 as much as 40 DU near in the tropopause region, while underestimating . Additionally, stratospheric ozone columns were
445 underestimated by as much as up to 20 DU relative to ozonesonde measurements. These discrepancies are notably mitigated
446 in GEMS v3.0, with tropospheric biases reduced to within 10 DU and stratospheric biases to within 5 DU. At lower lower-
447 latitude sites, both GEMS v2.0 and v3.0 produce qualitatively similar ozone profiles, as the vertical structure shows relatively
448 weak seasonal variability and the tropopause altitude remains stable, making #the retrievals easier to constrain with a priori
449 information.

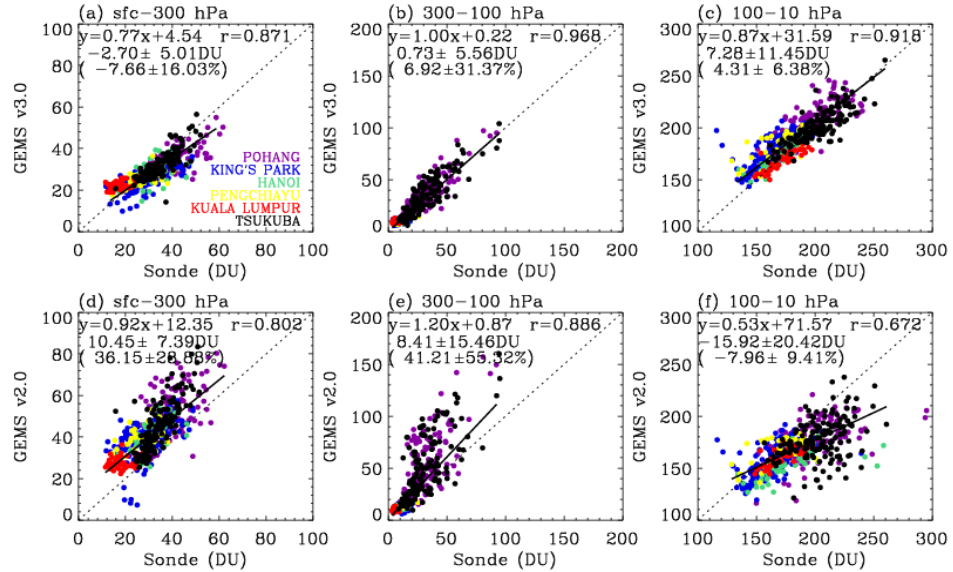
450 The retrieved ozone profiles from satellite nadir view observations generally exhibit weak vertical sensitivity, particularly
451 in the lower troposphere. The use of integrated column ozone is recommended to enhance the information content, as it allows
452 for a more practical validation compared to profile based approaches. Figure 10 presents time series comparisons of lower
453 tropospheric ozone columns (below 300 hPa) derived from GEMS (v2.0 in gray and v3.0 in black) and ozonesonde
454 observations (in red) at six stations across different latitudes during the period 2021 to 2024.



456
457 **Figure 10. Time-series of tropospheric ozone columns (surface-300 hPa) from GEMS v3.0 (black), GEMS v2.0 (grey),**
458 **and ozonesondes (red). The x-axis marks the months of the year using initials: J (January), A (April), J (July), and O**
459 **(October).**

460 Mid-latitude sites (Pohang and Tsukuba) exhibit pronounced seasonality, with ozonesonde-derived tropospheric ozone
461 columns ranging from 25 to 50 DU—peaking in summer and declining toward winter. Within the summer season, ozone levels
462 typically reach their maximum in June, followed by a sharp decline in July and August. As shown, GEMS v3.0 reasonably
463 reproduces this seasonal pattern. At subtropical sites such as Hanoi, King's Park, and Pengchiayu, seasonal changes are less
464 pronounced, with ozone columns typically fluctuating between 20 and 45 DU. A distinct spring peak of 40–45 DU is
465 consistently observed in both ozonesonde and GEMS v3.0 time-series. The lowest ozone levels are observed between July and
466 October, remaining a few DU lower than the wintertime minimum. At the tropical site of Kuala Lumpur, ozonesonde
467 measurements are limited in 2021 and 2022, but the available data suggest minimal seasonal variation in tropospheric ozone,
468 consistent with the weak seasonal signals typically observed in the tropics. With its dense temporal coverage, GEMS v3.0
469 complements the sparse ozonesonde measurements and identifies the flat tropospheric ozone levels throughout the 2021–2024
470 period. However, GEMS v2.0 systematically retrieves higher ozone levels across all latitudinal bands. This overestimation is
471 much more pronounced at mid-latitudes than at lower latitudes. In particular, GEMS v2.0 significantly overestimates summer
472 ozone values by 30 DU compared to GEMS v3.0, with the discrepancy decreasing toward winter. In the subtropics, the
473 difference between GEMS v2.0 and v3.0 remains about 15 DU, without clear seasonal change. In particular, GEMS v2.0
474 retrieves higher ozone amounts in 2023 and 2024 compared to earlier years, which is not reflected in either GEMS v3.0 or

475 ozonesonde data. This increasing discrepancy is likely associated with the optical degradation of the instrument, which leads
 476 to decreasing irradiance values over time (Kang et al. 2024; Bak et al. 2025b) and, in turn, affects the accuracy of the ozone
 477 profile retrievals. In the tropics, the GEMS products from both versions agree within 5 DU during 2021–2022, but the
 478 difference increases to within 10 DU in 2023–2024. Notably, the issues identified in GEMS v2.0 are substantially mitigated
 479 in GEMS v3.0, owing to the newly implemented radiometric calibration applied to both irradiance and normalized radiance.



480
 481 **Figure 11. Scatter plots of GEMS and ozonesonde ozone columns for three different layers, surface-300 hPa, 300-100
 482 hPa, and 100-10 hPa. The upper (a-c) panels show results from GEMS v3.0, and the bottom panels (d-f) from GEMS
 483 v2.0. Each data pair is color-coded by station. Regression lines and correlation coefficients (r) are derived from all data
 484 pairs, along with the mean bias and standard deviation reported in both DU and percentage.**

485

486 The quantitative comparison between GEMS and ozonesonde measurements is presented in Figure 11 (a, d) for
 487 tropospheric ozone columns below 300 hPa. Compared to version 2.0, which exhibits a substantial positive bias of 36.15%
 488 and high variability ($\pm 28.88\%$), GEMS v3.0 shows a marked improvement, reducing the bias to -7.66% with lower scatter
 489 ($\pm 16.03\%$) and achieving a higher correlation with ozonesonde observations ($r = 0.87$ vs. $r = 0.80$). The regression slope for
 490 GEMS v2.0 is closer to unity than that of v3.0, due to the presence of both negative biases at high-ozone sites and positive
 491 biases at low-ozone sites, whereas v2.0 shows more uniform positive biases across stations. Figure 11 also evaluates ozone
 492 partial columns in upper troposphere and lower stratosphere (UTLS: 300-100 hPa) and the middle stratosphere (100-10 hPa),
 493 respectively. The 100–10 hPa layer, which corresponds to the ozone maximum in the upper stratosphere, also shows good
 494 agreement, with GEMS v3.0 achieving a correlation of $r = 0.92$ and a relatively small mean bias ($4.31 \pm 6.38 \%$), further
 495 supporting the reliability of the updated retrievals at higher altitudes.

496 The GEMS retrievals are inherently more influenced by a priori information compared to existing nadir satellite products
497 such as OMI and TROPOMI, due to the narrower spectral range (310-330 nm versus 270-330 nm). Despite both versions
498 employing the same a priori constraints, GEMS v2.0 exhibits poorer agreement with ozonesonde data than the a priori itself,
499 reflecting the detrimental impact of radiometric uncertainties on the retrievals. However, GEMS v3.0 demonstrates better
500 agreement than the a priori, indicating improved retrieval performance, especially when retrieving high ozone concentrations
501 in both the troposphere and stratosphere. A comparison between GEMS a priori and ozonesondes is provided in Supplement
502 Figure 4.

503 **4.2 Validation with Asia-AQ campaign ozonesonde soundings**

504 ~~In Figure 12a shows the date-altitude cross-section of ozone mixing ratios profiles obtained from ozonesondes during the~~
505 ~~Asia AQ campaign at Seosan (February) and Kongju (March) during the 2024 Asia-AQ campaign. As the two sites are only~~
506 ~~about 131 km apart, they are treated jointly in the analysis and considered to represent similar ozone seasonality. Given that~~
507 ~~the two sites are located approximately 131 km apart, they can be considered to exhibit similar ozone seasonality. Figure 12,~~
508 ~~the ozonesonde measurements are presented as ozone mixing ratio profiles.~~ Ozone concentrations near the surface range from
509 30 to 50 ppb, which are lower than those in the upper troposphere—approximately 60 ppb in February and increasing to 80
510 ppb in March. These observed ~~tropospheric~~ ozone structures and their temporal variations are consistently reproduced from
511 GEMS v3.0 retrievals ~~collocated at Seosan in February and Kongju in March (Fig. 12b).~~ Notably, during the ~~absent of~~
512 ozonesonde ~~measurements~~~~data gap~~ in early March, GEMS v3.0 provides valuable supplementary information, revealing a
513 downward propagation of ozone-rich air from the upper to the lower troposphere over time. Above the tropopause (~ 10 km),
514 ozone mixing ratios generally exceed 0.1 ppm. The superimposed potential temperature profiles remained temporally stable
515 in the stratosphere, reflecting persistent stratification and limited vertical dynamical activity. However, ozone mixing ratios in
516 the lower stratosphere, particularly below 15 km, exhibited marked variability between 0.3 and 0.5 ppm, likely associated with
517 isentropic transport. GEMS v3.0 effectively captures these variations, ~~with demonstrating~~ enhanced ability to resolve ozone
518 fluctuations in the lower stratosphere. ~~However, as shown in Fig 12c, GENS compared to v2.0, which shows produces~~
519 smoother, less structured patterns.

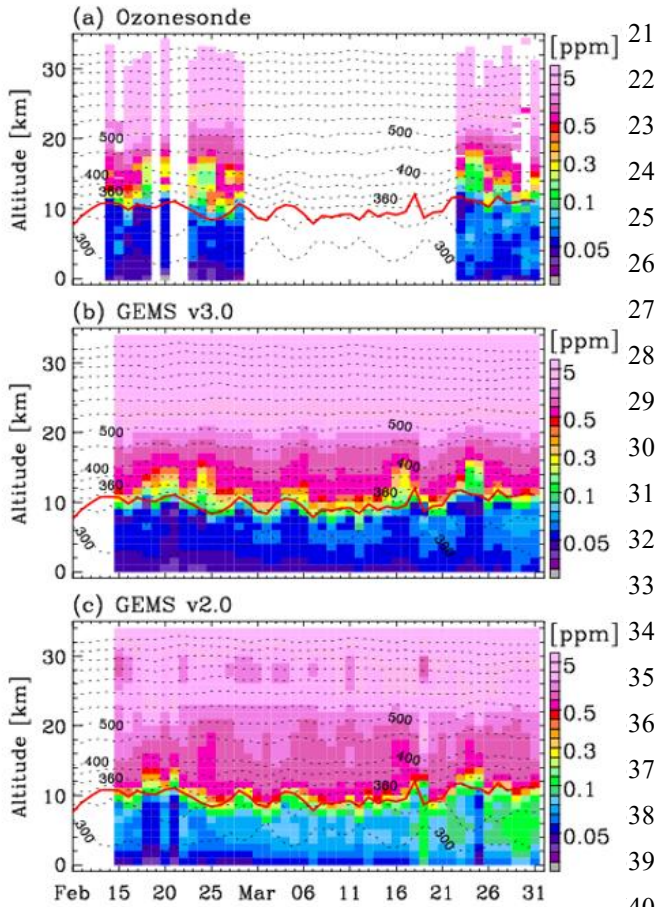
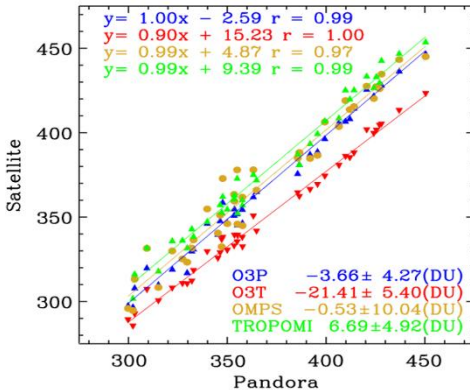


Figure 12. Time series of daily ozone mixing ratio profiles from ozonesondes and GEMS (v3.0 and v2.0) during the 2024 Asia-AQ campaign. The red line denotes the thermal tropopause, while the black contour lines (at 50 K intervals) represent potential temperatures, derived from the FNL meteorological product.

The evaluation of integrated ozone profiles as total ozone can provide useful insight into the overall accuracy and consistency of vertical profile retrievals when compared with well-established ground-based total column measurements (Bak et al., 2015). Ground-based Pandora total ozone column measurements at Seosan ([Park and Cede, 2025](#)) are used as a reference to evaluate the total ozone integrated from GEMS ozone profiles during the Asia-AQ campaign (Figure 13). An intercomparison of total ozone columns from GEMS (Baek et al., 2023), OMPS (Jaross, 2017), and TROPOMI ([Copernicus Sentinel-5P, 2020](#)[Garane et al., 2019](#)) is also included to assess the consistency between GEMS ozone products (O_3P and O_3T) and to evaluate the relative performance of GEMS compared to other satellite observations. As shown, total ozone values recorded by Pandora ranged from 300 to 450 DU during February and March 2024. These records closely align with satellite observations, evidenced by correlation coefficients of 0.97 or higher across all products. However, the retrievals from GEMS O_3T show inconsistent performance between low and high ozone levels, resulting in a regression slope of 0.9, whereas the other satellite products exhibit slopes close to unity. GEMS O_3T also significantly underestimates Pandora measurements, with a mean bias of -20 DU, primarily due to uncertainties in irradiance calibration (Baek et al., 2023). The scatter in the OMPS total ozone comparison is larger than that of the other products—by a factor of two—likely due to its coarse spatial resolution. GEMS O_3P shows better agreement than the other satellite products, both in terms of scatter and biases, with mean differences ranging from 1.5 to 8 DU (-3.66 ± 4.27 DU).



552
 553 **Figure 13.** Scatter plots of total ozone columns ~~retrieved~~ from ~~satellite observations~~ (GEMS O₃P, GEMS O₃T, OMPS, and
 554 ~~TROPOMI~~) against Pandora measurements at Seosan during February–March 2024. A total of 44 Pandora observation days was
 555 available, of which 42 remained after quality control. Regression lines ($y = \text{slope} \cdot x + \text{intercept}$) and correlation coefficients (r) are
 556 shown in the top legend, legend, and while the bottom legend presents mean bias $\pm 1\sigma$ for each product in the bottom legend. For
 557 comparison, Pandora observations are averaged within ± 30 min of 04:45 UTC each day and the satellite-Pandora pairs are were
 558 selected based on the nearest satellite pixel located within 100 km of the Pandora site.

559
 560 **5. Conclusions for Version 3 and Remarks for the Next Version**

561 This study provides the first detailed description of the GEMS operational ozone profile retrieval algorithm in the
 562 literature, along with an analysis of its retrieval characteristics in the 310–330 nm spectral range. The vertical sensitivity of the
 563 GEMS ozone profile is close to unity throughout most of the atmosphere. A decrease to values below 0.5 is observed only in
 564 the lowest five km. Outside of the lower stratosphere (about 15–30 km), the vertical sensitivity is mostly found off-diagonal,
 565 resulting in a rather low average retrieval DFS of about 1.5, up to 3 at maximum. The effective vertical resolution of the GEMS
 566 O₃P retrieval amounts to 5–10 km.

567 This work primarily highlights substantial algorithmic and calibration enhancements implemented in version 3.0 over
 568 the previous version. Unlike other Level 2 algorithms that typically assume a uniform spectral shift, this work accounts for
 569 independent spectral shifts in radiance and irradiance. To address significant irradiance offsets—arising spatially and
 570 seasonally from BTDF-induced effects, and temporally from optical component degradation—a scaling factor correction is
 571 introduced. This scaling factor basically represents the ratio between the measured irradiance and the solar reference, capturing
 572 systematic deviations due to calibration limitations. Additionally, a soft calibration is applied to compensate for residual
 573 wavelength-dependent uncertainties not addressed by the scaling factor, as well as for spatial (cross-track) variations in
 574 normalized radiance. The GEMS soft spectra are derived from clear-sky observations during the week of July 11–17, 2021,
 575 at 02:45 UTC, to address systematic residuals between measured and simulated normalized radiances as a function of spatial
 576 pixel, and are applied uniformly across all observation times. We also adopt the newly implemented forward model, additional
 577 fitting parameters, and auxiliary data from the OMI Collection 4 ozone profile algorithm (Bak et al., 2024). As a result, version

578 3.0 achieves a spectral fitting residual of 0.2% (low SZA/VZA) in ozone profile retrievals, indicating a fourfold improvement
579 compared to version 2.0. Validation results further confirm the improved performance of the version 3.0 ozone profile product.
580 Comparisons with regular ozonesonde observations from six East and Southeast Asian stations reveal substantial bias reduction
581 and improved consistency in both the troposphere and lower stratosphere, effectively smoothing the altitude-dependent
582 oscillating biases observed in version 2.0. The mean tropospheric ozone column bias is reduced from +36.2% in version 2.0
583 to -7.7% in version 3.0, accompanied by an improvement in ~~with~~ the correlation coefficient from improved from 0.80 to 0.87.
584 Stratospheric retrievals also show good agreement, with a mean bias of 4.3% and a correlation coefficient of 0.92. Time series
585 comparisons of tropospheric ozone demonstrate a better representation of the seasonal cycle in version 3.0, whereas version
586 2.0 exhibited an artificial increasing trend. Additional validation using ozonesonde data from the 2024 Asia-AQ campaign
587 supports the improved vertical structure and day-to-day variability captured by GEMS version 3.0. Furthermore, GEMS total
588 ozone columns derived from version 3.0 profiles show excellent agreement with Pandora measurements ($r = 0.99$, mean bias=
589 -3.7 DU), outperforming the GEMS total ozone product. The reprocessing of the GEMS ozone profile dataset has been
590 completed and the version 3 product is publicly available through the Environmental Satellite Center website
591 (<https://nesc.nier.go.kr/en/html/datasvc/index.do>; NIER, 2025).

592 In this study, we focused on the afternoon measurements at 04:45 UTC (13:45 local time, KST), which correspond to
593 the overpass time of polar-orbiting satellites in East Asia. In the next version (version 4), we will aim to improve and validate
594 the ozone profile product for hourly observations. Irradiance calibration will be enhanced by accounting for BTDF effects and
595 optical degradation in the Level 1C processing, which is expected to provide a more robust foundation for both ozone profile
596 retrievals and auxiliary input data such as total ozone and cloud information. In turn, the use of soft spectra will be extended
597 to support hourly, seasonal, and yearly applications, enabling improved temporal consistency in the quality of the GEMS ozone
598 profile product for both diurnal variation analysis and long-term atmospheric monitoring.

599 Acknowledgements

600 We thank the GEMS science team and the Environmental Satellite Center (ESC) of the National Institute of Environmental
601 Research (NIER) for their support in the development of the GEMS ozone profile retrieval algorithm. We also acknowledge
602 the contributions of the TEMPO, ESA PEGASUS, and ASIA-AQ, WOUDC, SHADOZ teams to algorithm improvements and
603 product validation.

604

605 **Competing interests.** The authors have no competing interests

606

607 Code availability

608 The GEMS L2 O₃P algorithm is not available publicly.

609 **Data availability**

610 GEMS L2 O3P data can be obtained from the Environmental Satellite Center website
611 (<https://nesc.nier.go.kr/en/html/datasvc/index.do>; NIER, 2025) ([current version is 3.0 for entire mission](#)). The Asia-AQ
612 campaign archives are available from <https://www-air.larc.nasa.gov/missions/asia-aq/> (NASA, 2023). The regular ozonesonde
613 observations are downloaded from the WOUDC, SHADOZ, and KMA websites.

614

615 **Financial support**

616 This research was supported by Basic Science Research Program through the National Research Foundation of Korea
617 (NRF) funded by the Ministry of Education (grant no. 2020R1A6A1A03044834 and 2021R1A2C1004984). Additional
618 support was provided by a grant from the National Institute of Environment Research (NIER), funded by the Ministry of
619 Environment (MOE) of the Republic of Korea (grant no. NIER-2025-04-02-063). GEMS O3P retrieval characterization and
620 validation studies were performed within the PEGASOS (Product Evaluation of GEMS L2 via Assessment with S5P and Other
621 Sensors) project funded by the European Space Agency (ESA) (contract No. 4000138176/22/I-DT-1r). X.L. and G.G.A were
622 supported by the NASA TEMPO project (Contract No. NNL13AA09C); as well as the NASA Grant 80NSSC19K1626.

623

624 **Author Contributions** J.B., D.C., J.K. (Jae-Hwan Kim), X.L., and K.Y. developed the ozone profile retrieval algorithm.
625 G.G.A. developed the radiance data reading modules. A.K. and J.C.L. performed the retrieval characterization. J.H.K. (Ja-Ho
626 Koo) and J.K. (Joowan Kim) provided the Asia-AQ ozonesonde data. S.H., K.B., Y.J and K.P.H. conducted the validation.
627 C.H.K., H.L., and W.J. advised on the implementation of meteorological reanalysis and forecast data. J.K. (Jhoon Kim) led
628 the overall GEMS project. H.H. and W.L. managed the project. All authors contributed to the data analysis and manuscript
629 preparation.

630

631 **References**

632

633 Baek, K., Kim, J. H., Bak, J., Haffner, D. P., Kang, M. and Hong, H.: Evaluation of total ozone measurements from
634 Geostationary Environmental Monitoring Spectrometer (GEMS), *Atmos. Meas. Tech.*, 16(22), 5461–5478,
635 doi:10.5194/amt-16-5461-2023, 2023.

636 Baek, K., Bak, J., Kim, J. H., Park, S. S., Haffner, D. P. and Lee, W.: Validation of geostationary environment monitoring
637 spectrometer (GEMS), TROPOspheric Monitoring Instrument (TROPOMI), and Ozone Mapping and Profiler Suite
638 Nadir Mapper (OMPS) using pandora measurements during GEMS Map of Air Pollution (GMAP) field campaign,
639 *Atmos. Environ.*, 324(August 2023), 120408, doi:10.1016/j.atmosenv.2024.120408, 2024.

640 Bak, J., Liu, X., Wei, J. C., Pan, L. L., Chance, K. and Kim, J. H.: Improvement of omi ozone profile retrievals in the upper
641 troposphere and lower stratosphere by the use of a tropopause-based ozone profile climatology, *Atmos. Meas. Tech.*,
642 6(9), 2239–2254, doi:10.5194/amt-6-2239-2013, 2013.

643 Bak, J., Liu, X., Kim, J. H., Chance, K. and Haffner, D. P.: Validation of OMI total ozone retrievals from the SAO ozone
644 profile algorithm and three operational algorithms with Brewer measurements, *Atmos. Chem. Phys.*, 15(2), 667–683,
645 doi:10.5194/acp-15-667-2015, 2015.

646 Bak, J., Liu, X., Kim, J.-H., Haffner, D. P., Chance, K., Yang, K. and Sun, K.: Characterization and correction of OMPS nadir
647 mapper measurements for ozone profile retrievals, *Atmos. Meas. Tech.*, 10(11), 4373–4388, doi:10.5194/amt-10-4373-
648 2017, 2017.

649 Bak, J., Kim, J. H., Nam, H., Baek, K. and Shin, D.: Geostationary Environment Monitoring Spectrometer (GEMS) Algorithm
650 Theoretical Basis Document Ozone Profile Retrieval Algorithm, , (April), 10–11 [online] Available from:
651 <https://nesc.nier.go.kr/ko/html/satellite/doc/doc.do>, 2020.

652 Bak, J., Liu, X., Spurr, R., Yang, K., Nowlan, C. R., Miller, C. C., Abad, G. G. and Chance, K.: Radiative transfer acceleration
653 based on the principal component analysis and lookup table of corrections: optimization and application to UV ozone
654 profile retrievals, *Atmos. Meas. Tech.*, 14(4), 2659–2672, doi:10.5194/amt-14-2659-2021, 2021.

655 Bak, J., Song, E.-J., Lee, H.-J., Liu, X., Koo, J.-H., Kim, J., Jeon, W., Kim, J.-H. and Kim, C.-H.: Temporal variability of
656 tropospheric ozone and ozone profiles in the Korean Peninsula during the East Asian summer monsoon: insights from
657 multiple measurements and reanalysis datasets, *Atmos. Chem. Phys.*, 22(21), 14177–14187, doi:10.5194/acp-22-
658 14177-2022, 2022.

659 Bak, J., Liu, X., Yang, K., Gonzalez Abad, G., O’Sullivan, E., Chance, K. and Kim, C.-H.: An improved OMI ozone profile
660 research product version 2.0 with collection 4 L1b data and algorithm updates, *Atmos. Meas. Tech.*, 17(7), 1891–1911,
661 doi:10.5194/amt-17-1891-2024, 2024.

662 Bak, J., Liu, X., Abad, G. G. and Yang, K.: An Extension of Ozone Profile Retrievals from TROPOMI Based on the SAO2024
663 Algorithm, *Remote Sens.*, 17(5), doi:10.3390/rs17050779, 2025a.

664 Birk, M. and Wagner, G.: ESA SEOM-IAS – Measurement and ACS database O3 UV region, ,
665 doi:10.5281/ZENODO.1485588, 2018.

666 Brion, J., Chakir, A., Daumont, D., Malicet, J. and Parisse, C.: High-resolution laboratory absorption cross section of O3.
667 Temperature effect, *Chem. Phys. Lett.*, 213(5), 610–612, doi:[https://doi.org/10.1016/0009-2614\(93\)89169-I](https://doi.org/10.1016/0009-2614(93)89169-I), 1993.

668 Cai, Z., Liu, Y., Liu, X., Chance, K., Nowlan, C. R., Lang, R., Munro, R. and Suleiman, R.: Characterization and correction of
669 global ozone monitoring experiment 2 ultraviolet measurements and application to ozone profile retrievals, *J. Geophys.
670 Res. Atmos.*, 117(7), 1–16, doi:10.1029/2011JD017096, 2012.

671 Chance, K. and Kurucz, R. L.: An improved high-resolution solar reference spectrum for earth’s atmosphere measurements in
672 the ultraviolet, visible, and near infrared, *J. Quant. Spectrosc. Radiat. Transf.*, 111(9), 1289–1295,
673 doi:10.1016/j.jqsrt.2010.01.036, 2010.

674 Coddington, O. M., Richard, E. C., Harber, D., Pilewskie, P., Woods, T. N., Chance, K., Liu, X. and Sun, K.: The TSIS-1
675 Hybrid Solar Reference Spectrum, *Geophys. Res. Lett.*, 1–10, doi:10.1029/2020gl091709, 2021.

676 Daumont, D., Brion, J., Charbonnier, J. and Malicet, J.: Ozone UV spectroscopy I: Absorption cross-sections at room
677 temperature, *J. Atmos. Chem.*, 15(2), 145–155, doi:10.1007/BF00053756, 1992.

678 Van Dingenen, R., Dentener, F. J., Raes, F., Krol, M. C., Emberson, L. and Cofala, J.: The global impact of ozone on
679 agricultural crop yields under current and future air quality legislation, *Atmos. Environ.*, 43(3), 604–618,
680 doi:<https://doi.org/10.1016/j.atmosenv.2008.10.033>, 2009.

681 Dobber, M., Voors, R., Dirksen, R., Kleipool, Q. and Levelt, P.: The high-resolution solar reference spectrum between 250
682 and 550 nm and its application to measurements with the ozone monitoring instrument, *Sol. Phys.*, 249(2), 281–291,
683 doi:10.1007/s11207-008-9187-7, 2008.

684 Garane, K., Koukouli, M.-E., Verhoelst, T., Lerot, C., Heue, K.-P., Fioletov, V., Balis, D., Bais, A., Bazureau, A., Dehn, A.,
685 Goutail, F., Granville, J., Griffin, D., Hubert, D., Keppens, A., Lambert, J.-C., Loyola, D., McLinden, C., Pazmino, A.,
686 Pommereau, J.-P., Redondas, A., Romahn, F., Valks, P., Van Roozendael, M., Xu, J., Zehner, C., Zerefos, C. and
687 Zimmer, W.: TROPOMI/S5P total ozone column data: global ground-based validation and consistency with other
688 satellite missions, *Atmos. Meas. Tech.*, 12(10), 5263–5287, doi:10.5194/amt-12-5263-2019, 2019.

689 Hayashida, S., Liu, X., Ono, A., Yang, K. and Chance, K.: Observation of ozone enhancement in the lower troposphere over
690 East Asia from a space-borne ultraviolet spectrometer, *Atmos. Chem. Phys.*, 15(17), 9865–9881, doi:10.5194/acp-15-
691 9865-2015, 2015.

692 Isaksen, I. S. A., Granier, C., Myhre, G., Berntsen, T. K., Dalsøren, S. B., Gauss, M., Klimont, Z., Benestad, R., Bousquet, P.,
693 Collins, W., Cox, T., Eyring, V., Fowler, D., Fuzzi, S., Jöckel, P., Laj, P., Lohmann, U., Maione, M., Monks, P.,
694 Prevot, A. S. H., Raes, F., Richter, A., Rognerud, B., Schulz, M., Shindell, D., Stevenson, D. S., Storelvmo, T., Wang,
695 W.-C., van Weele, M., Wild, M. and Wuebbles, D.: Atmospheric composition change: Climate–Chemistry interactions,
696 *Atmos. Environ.*, 43(33), 5138–5192, doi:<https://doi.org/10.1016/j.atmosenv.2009.08.003>, 2009.

697 Kang, M., Ahn, M. H., Ko, D. H., Kim, J., Nicks, D., Eo, M., Lee, Y., Moon, K. J. and Lee, D. W.: Characteristics of the
698 Spectral Response Function of Geostationary Environment Monitoring Spectrometer Analyzed by Ground and In-Orbit
699 Measurements, *IEEE Trans. Geosci. Remote Sens.*, 60, 1–16, doi:10.1109/TGRS.2021.3091677, 2022.

700 Kang, M., Ahn, M.-H., Lee, Y., Ho Ko, D., Eo, M., Kim, J. and Moon, K.-J.: On-Orbit Correction of Bi-Directional
701 Transmittance Distribution Function (BTDF) of Geostationary Environment Monitoring Spectrometer (GEMS), *IEEE*
702 *Trans. Geosci. Remote Sens.*, 62, 1–15, doi:10.1109/TGRS.2024.3510337, 2024.

703 Keppens, A., Lambert, J.-C., Granville, J., Miles, G., Siddans, R., van Peet, J. C. A., van der A, R. J., Hubert, D., Verhoelst,
704 T., Delcloo, A., Godin-Beekmann, S., Kivi, R., Stübi, R. and Zehner, C.: Round-robin evaluation of nadir ozone profile
705 retrievals: methodology and application to MetOp-A GOME-2, *Atmos. Meas. Tech.*, 8(5), 2093–2120,
706 doi:10.5194/amt-8-2093-2015, 2015.

707 Kim, J., Jeong, U., Ahn, M.-H., Kim, J. H., Park, R. J., Lee, H., Song, C. H., Choi, Y.-S., Lee, K.-H., Yoo, J.-M., Jeong, M.-J.,
708 Park, S. K., Lee, K.-M., Song, C.-K., Kim, S.-W., Kim, Y. J., Kim, S.-W., Kim, M., Go, S., Liu, X., Chance, K., Miller,
709 C. C., Al-Saadi, J., Veihelmann, B., Bhartia, P. K., Torres, O., Abad, G. G., Haffner, D. P., Ko, D. H., Lee, S. H., Woo,

710 J.-H., Chong, H., Park, S. S., Nicks, D., Choi, W. J., Moon, K.-J., Cho, A., Yoon, J., Kim, S., Hong, H., Lee, K., Lee,
711 H., Lee, S., Choi, M., Veefkind, P., Levelt, P. F., Edwards, D. P., Kang, M., Eo, M., Bak, J., Baek, K., Kwon, H.-A.,
712 Yang, J., Park, J., Han, K. M., Kim, B.-R., Shin, H.-W., Choi, H., Lee, E., Chong, J., Cha, Y., Koo, J.-H., Irie, H.,
713 Hayashida, S., Kasai, Y., Kanaya, Y., Liu, C., Lin, J., Crawford, J. H., Carmichael, G. R., Newchurch, M. J., Lefer, B.
714 L., Herman, J. R., Swap, R. J., Lau, A. K. H., Kurosu, T. P., Jaross, G., Ahlers, B., Dobber, M., McElroy, C. T. and
715 Choi, Y.: New Era of Air Quality Monitoring from Space: Geostationary Environment Monitoring Spectrometer
716 (GEMS), *Bull. Am. Meteorol. Soc.*, 101(1), E1–E22, doi:10.1175/BAMS-D-18-0013.1, 2020.

717 Kim, J. H., Baek, K. and Lee, H.: Geostationary Environment Monitoring Spectrometer (GEMS) Algorithm Theoretical Basis
718 Document Total Column Ozone Retrieval Algorithm, , (December) [online] Available from:
719 <https://nesc.nier.go.kr/ko/html/satellite/doc/doc.do>, 2024.

720 Kuang, S., Newchurch, M. J., Johnson, M. S., Wang, L., Burris, J., Pierce, R. B., Eloranta, E. W., Pollack, I. B., Graus, M., de
721 Gouw, J., Warneke, C., Ryerson, T. B., Markovic, M. Z., Holloway, J. S., Pour-Biazar, A., Huang, G., Liu, X. and
722 Feng, N.: Summertime tropospheric ozone enhancement associated with a cold front passage due to stratosphere-to-
723 troposphere transport and biomass burning: Simultaneous ground-based lidar and airborne measurements, *J. Geophys.
724 Res. Atmos.*, 122(2), 1293–1311, doi:<https://doi.org/10.1002/2016JD026078>, 2017.

725 Lee, K., Lee, D.-W., Chang, L.-S., Yu, J.-A., Lee, W.-J., Kang, K.-H. and Jeong, J.: Pioneering Air Quality Monitoring over
726 East and Southeast Asia with the Geostationary Environment Monitoring Spectrometer (GEMS), *Korean J. Remote
727 Sens.*, 40(5), 741–752, doi:10.7780/kjrs.2024.40.5.2.5, 2024.

728 Liu, X., Chance, K., Sioris, C. E., Spurr, R. J. D., Kurosu, T. P., Martin, R. V. and Newchurch, M. J.: Ozone profile and
729 tropospheric ozone retrievals from the Global Ozone Monitoring Experiment: Algorithm description and validation, *J.
730 Geophys. Res.*, 110(D20), D20307, doi:10.1029/2005JD006240, 2005.

731 Liu, X., Bhartia, P. K., Chance, K., Spurr, R. J. D. and Kurosu, T. P.: Ozone profile retrievals from the Ozone Monitoring
732 Instrument, *Atmos. Chem. Phys.*, 10(5), 2521–2537, doi:10.5194/acp-10-2521-2010, 2010.

733 Lu, X., Zhang, L., Liu, X., Gao, M., Zhao, Y. and Shao, J.: Lower tropospheric ozone over India and its linkage to the South
734 Asian monsoon, *Atmos. Chem. Phys.*, 18(5), 3101–3118, doi:10.5194/acp-18-3101-2018, 2018.

735 Malicet, J., Daumont, D., Charbonnier, J., Parisse, C., Chakir, A. and Brion, J.: Ozone UV spectroscopy. II. Absorption cross-
736 sections and temperature dependence, *J. Atmos. Chem.*, 21(3), 263–273, doi:10.1007/BF00696758, 1995.

737 McPeters, R. D. and Labow, G. J.: Climatology 2011: An MLS and sonde derived ozone climatology for satellite retrieval
738 algorithms, *J. Geophys. Res. Atmos.*, 117(D10), doi:<https://doi.org/10.1029/2011JD017006>, 2012.

739 Monks, P. S., Archibald, A. T., Colette, A., Cooper, O., Coyle, M., Derwent, R., Fowler, D., Granier, C., Law, K. S., Mills, G.
740 E., Stevenson, D. S., Tarasova, O., Thouret, V., von Schneidemesser, E., Sommariva, R., Wild, O. and Williams, M. L.:
741 Tropospheric ozone and its precursors from the urban to the global scale from air quality to short-lived climate forcer,
742 *Atmos. Chem. Phys.*, 15(15), 8889–8973, doi:10.5194/acp-15-8889-2015, 2015.

743 Rodgers, C. D.: Inverse Methods for Atmospheric Sounding, WORLD SCIENTIFIC., 2000.

744 Solomon, S.: Stratospheric ozone depletion: A review of concepts and history, Rev. Geophys., 37(3), 275–316,
745 doi:<https://doi.org/10.1029/1999RG900008>, 1999.

746 Zhao, F., Liu, C., Cai, Z., Liu, X., Bak, J., Kim, J., Hu, Q., Xia, C., Zhang, C., Sun, Y., Wang, W. and Liu, J.: Ozone profile
747 retrievals from TROPOMI: Implication for the variation of tropospheric ozone during the outbreak of COVID-19 in
748 China, Sci. Total Environ., 764, 142886, doi:[10.1016/j.scitotenv.2020.142886](https://doi.org/10.1016/j.scitotenv.2020.142886), 2021.

749

750

751 <references which is added manually>

752 NASA: *Draft Planning Document for ASIA-AQ*, available at:
753 https://espo.nasa.gov/sites/default/files/documents/Draft%20Planning%20Document%20for%20ASIA-AQ_20230720.pdf (last access: [20 August 2025](#)[14 May 2025](#)), 2023.

754 National Institute of Environmental Research (NIER): GEMS data, Environmental Satellite Center [data set], available at:
755 <https://nesc.nier.go.kr/en/html/datasvc/index.do> (last access: [20 August 2025](#)[14 May 2025](#)).

756 Livesey, N. J., Read, W. G., Wagner, P. A., Froidevaux, L., Santee, M. L., Schwartz, M. J., Lambert, A., Millán Valle, L. F.,
757 Pumphrey, H. C., Manney, G. L., et al.: EOS MLS Version 5.0x Level 2 and 3 Data Quality and Description Document,
758 Tech. Rep., Jet Propulsion Laboratory, D-105336 Rev. B, 30 January 2022, available at: <https://mls.jpl.nasa.gov/eos-aura-mls/documentation.php> (last access: [20 August 2025](#)[14 May 2025](#)).

759 Jaross, G.: OMPS-NPP L2 NM Ozone (O₃) Total Column Swath Orbital V2, Goddard Earth Sciences Data and Information
760 Services Center (GES DISC), Greenbelt, MD, USA, <https://doi.org/10.5067/0WF4HAAZ0VHK>, last access: [20 August 2025](#)[14 May 2025](#).

761 *Copernicus Sentinel-5P (processed by ESA), 2020, TROPOMI Level 2 Ozone Total Column products. Version 02. European Space Agency.* <https://doi.org/10.5270/S5P-ft13p57>, last access: [1420 August 2025](#).

762 Bak, J., et al.: Geostationary Environment Monitoring Spectrometer (GEMS): Long-Term Radiometric Accuracy and Spectral
763 Stability from 4.5 years of In-Orbit Solar Irradiance Observations, in review, IEEE Trans. Geosci. Remote Sens., 2025b.

764 Park, J. and Cede, A.: Pandora total ozone column data at Seosan (P164s1), Institute of Atmospheric Environment, Chungcheong
765 Province, Republic of Korea, <https://doi.org/10.48956/pgn.rout2p1-8.Seosan.P164s1>, last access: [20 May](#)[August 2025](#).

766

767

768

769

770